



Contents lists available at ScienceDirect

Journal of the Mechanics and Physics of Solids

journal homepage: www.elsevier.com/locate/jmps

Review Article

Revisiting nucleation in the phase-field approach to brittle fracture

Aditya Kumar^a, Blaise Bourdin^b, Gilles A. Francfort^{c,d}, Oscar Lopez-Pamies^{a,*}^a Department of Civil and Environmental Engineering, University of Illinois, Urbana-Champaign, IL 61801, USA^b Department of Mathematics, Louisiana State University, Baton Rouge, LA 70803, USA^c Courant Institute of Mathematical Sciences, 251 Mercer Street, New York, NY 10012, USA^d LAGA, Université Paris-Nord, Avenue J.-B. Clément 93430 – Villetaneuse, France

ARTICLE INFO

Article history:

Received 17 April 2020

Accepted 8 May 2020

Available online 20 May 2020

Keywords:

Fracture

Strength

Energy methods

Configurational forces

Brittle materials

ABSTRACT

Twenty years in since their introduction, it is now plain that the regularized formulations dubbed as phase-field of the variational theory of brittle fracture of Francfort and Marigo (1998) provide a powerful macroscopic theory to describe and predict the propagation of cracks in linear elastic brittle materials under arbitrary quasistatic loading conditions. Over the past ten years, the ability of the phase-field approach to also possibly describe and predict crack nucleation has been under intense investigation. The first of two objectives of this paper is to establish that the existing phase-field approach to fracture at large – irrespectively of its particular version – cannot possibly model crack nucleation. This is so because it lacks one essential ingredient: the strength of the material.

The second objective is to amend the phase-field theory in a manner such that it can model crack nucleation, be it from large pre-existing cracks, small pre-existing cracks, smooth and non-smooth boundary points, or within the bulk of structures subjected to arbitrary quasistatic loadings, while keeping undisturbed the ability of the standard phase-field formulation to model crack propagation. The central idea is to implicitly account for the presence of the inherent microscopic defects in the material – whose defining macroscopic manifestation is precisely the strength of the material – through the addition of an external driving force in the equation governing the evolution of the phase field. To illustrate the descriptive and predictive capabilities of the proposed theory, the last part of this paper presents sample simulations of experiments spanning the full range of fracture nucleation settings.

© 2020 The Author(s). Published by Elsevier Ltd.
This is an open access article under the CC BY-NC-ND license.
(<http://creativecommons.org/licenses/by-nc-nd/4.0/>)

1. Introduction

From its inception at the hands of A.A. Griffith (1921) onward fracture mechanics' foremost concern has been crack propagation. Griffith's main conceptual tenet was a cost-benefit analysis of the state of the crack – truly, in his mind, the

* Corresponding author.

E-mail addresses: akumar51@illinois.edu (A. Kumar), bourdin@lsu.edu (B. Bourdin), gilles.francfort@cims.nyu.edu, gilles.francfort@univ-paris13.fr (G.A. Francfort), pamies@illinois.edu (O. Lopez-Pamies).

crack length along a pre-assigned crack path — at any given time. Simply put, the crack has a given length at that time because having a longer crack would cost more surface energy that it would save in potential energy. As a consequence, he derived the notion of critical energy release rate as a necessary first order condition for his initial postulate. As such, the infamous $G \leq G_c$ was a mere by-product of Griffith's viewpoint. G. Irwin (1957) conferred a much higher status to that inequality when he related the energy release rate to the stress intensity factors. Doing so, he willingly, or unwillingly, steered the discipline into an increasingly inhospitable terrain, that of the computation of the K_I 's in various geometric, material, and load settings. J.R. Rice (1968) affirmed in turn the omnipotence of the energy release rate by equating it to various path-independent integrals arising out of material invariances. While both results had tremendous impact, they could not *per se* be the end-all of crack path prediction. They were simply a convenient tool for computing the energy release rate G . The community was then left to endlessly debate two main questions: is G always a meaningful object? And, if and when it is, is the notion (of uncertain origin) that crack motion will occur when G reaches its critical value G_c the key to crack path prediction?

Starting with the work of Francfort and Marigo (1998) in the late 1990/s and that of many others since, the focus of fracture mechanics was re-adjusted to be more in line with Griffith's original intent. The fracture state is now viewed as a minimization problem for the sum of the potential and surface energies with arbitrary add-cracks as test fields. There is no need to appeal to the notion of energy release rate. At the same time, an additional ingredient, energy conservation, forces crack evolution. In our undoubtedly biased view, this, absent inertia, is a closing chapter in the tormented history of crack propagation, at least as far as brittle materials are concerned.

In the most basic setting, that of an isotropic linear elastic material with stored-energy function $W(\mathbf{E}) := 1/2\{2\mu\mathbf{E} \cdot \mathbf{E} + \lambda(\text{tr } \mathbf{E})^2\}$ occupying an open bounded domain $\Omega \subset \mathbb{R}^N$, $N = 1, 2, 3$, the evolution, discretized in time for simplicity, goes as follows. Denote by G_c the critical elastic energy release rate and assume that $\bar{\mathbf{u}}$ is a time-dependent displacement prescribed on a part $\partial\Omega_D$ of the boundary. Then the displacement field $\mathbf{u}_k = \mathbf{u}_k(\mathbf{x})$ and crack set Γ_k within Ω at any given discrete time $t_k \in \{0 = t_0, t_1, \dots, t_m, t_{m+1}, \dots, t_M = T\}$ is determined by the minimization problem

$$(\mathbf{u}_k, \Gamma_k) = \arg \min_{\substack{\mathbf{u} = \bar{\mathbf{u}}(t_k) \text{ on } \partial\Omega_D \setminus \Gamma \\ \Gamma \supset \Gamma_{k-1}}} \mathcal{E}(\mathbf{u}, \Gamma) := \int_{\Omega \setminus \Gamma} W(\mathbf{E}(\mathbf{u})) \, d\mathbf{x} + G_c \mathcal{H}^{N-1}(\Gamma \cap \bar{\Omega} \setminus \partial\Omega_N). \quad (1)$$

In this expression, $\mathcal{H}^{N-1}(\Gamma)$ stands for the $(N-1)$ -dimensional Hausdorff measure (the surface measure) of the unknown crack Γ , $\partial\Omega_N = \partial\Omega \setminus \partial\Omega_D$, and $\mathbf{E}(\mathbf{u}) := 1/2(\nabla\mathbf{u} + \nabla\mathbf{u}^T)$ for the symmetrized gradient of the displacement field \mathbf{u} .

Many criticisms have been levied against this formulation through the years. Chief among them is the unrealistic assumption that the fields (\mathbf{u}_k, v_k) should be global minimizers. Equally bothersome, although less often alluded to, is the inability of such a formulation to cope with force loads in lieu of displacement loads. Many such issues are discussed at length in Bourdin et al. (2008). Such traverses notwithstanding, the formulation has proved very successful because it is amenable to approximation through regularized formulations that are often labeled “phase-field” approximations (Bourdin et al., 2000). A broad class¹ of such regularized minimization problems of (1) is given by

$$(\mathbf{u}_k^\varepsilon, v_k^\varepsilon) = \arg \min_{\substack{\mathbf{u} = \bar{\mathbf{u}}(t_k) \text{ on } \partial\Omega_D \\ 0 \leq v \leq v_{k-1} \leq 1}} \mathcal{E}^\varepsilon(\mathbf{u}, v) := \int_{\Omega} \psi(v) W(\mathbf{E}(\mathbf{u})) \, d\mathbf{x} + \frac{G_c}{4c_s} \int_{\Omega} \left(\frac{s(v)}{\varepsilon} + \varepsilon \nabla v \cdot \nabla v \right) \, d\mathbf{x}, \quad (2)$$

where $\varepsilon > 0$ is a regularization or localization length, v is an order parameter or phase-field variable taking values in $[0, 1]$, ψ and s are continuous monotonic functions such that $\psi(0) = 0$, $\psi(1) = 1$, $s(0) = 1$, $s(1) = 0$, and $c_s := \int_0^1 \sqrt{s(z)} \, dz$ is a normalization parameter; see, e.g., Braides (1998).

Any attempt at giving an overview of the various studies that have spawned out of this formulation would be a hopeless task. The many evolutions that have been generated so far through application of some form or other of (2) never follow globally minimizing paths but, at best, paths along critical points. This is so because of the lack of convexity of the functional $(\mathbf{u}, v) \mapsto \mathcal{E}^\varepsilon(\mathbf{u}, v)$. Since global minimality is unrealistic, evolutions along critical points could be deemed desirable but doing so has the unfortunate consequence that the link with the sharp theory contained in a formulation like (1) has been severed.

Summing up, a twist of fate asserts that well understood and correctly implemented versions of (2) accurately portray crack propagation for a wide variety of geometries, material parameters, and loading patterns.

But triumph, even of the blind sort, would be premature. To achieve such results the various practitioners of fracture evolution have to confront nucleation. Whenever a large pre-existing crack is present anything goes (within reason). In the absence of a precursor to propagation, however, the situation is muddy. The localization of the phase-field variable v is commonly seen as the manifestation of crack nucleation. A key issue there is that the localization of v is inherently an ε -dependent event. Because of this, numerous authors have promoted the idea that a meaningful nucleation can be obtained by fixing the value of ε to the “right” length scale. To obtain that value of ε , they typically resort to a one-dimensional

¹ As will become apparent in Sections 2 and 3, the conclusions of this paper remain applicable to the broader class of regularizations where only a “tensile” part $W^+(\mathbf{E}(\mathbf{u}))$ of the elastic energy $W(\mathbf{E}(\mathbf{u}))$ is multiplied by the degradation function $\psi(v)$; see, e.g., Lancioni and Royer-Carfigni (2009), Amor et al. (2009), Miehe et al. (2010), Chambolle et al. (2018).

traction test for which the maximal stress, or tensile strength, σ_{ts} is usually known and viewed as a material constant, and then adjust the length scale ε so that the phase field v for that test becomes incrementally unstable precisely for the value σ_{ts} of the traction; see, e.g., Amor et al. (2009), Pham et al. (2011), Borden et al. (2012), Mesgarnejad et al. (2015), Nguyen et al. (2016), Pham et al. (2017), Alessi et al. (2018), Tanné et al. (2018).

In this work, we first argue in Sections 2 and 3 that such remedies are insufficient because fracture nucleation cannot be properly modeled by the phase-field formulation (2). Indeed, the formulation (2) is purely energetic and as a result it cannot account for one essential ingredient that is intrinsically *not* energetic, but rather stress-based: *the strength of the material*. This point was evidenced in recent work of Kumar et al. (2018a) on rubber inspired by a detailed analysis by Lefèvre et al. (2015) of the classical experiments² of Gent and Lindley (1959) and Gent and Park (1984). In point of fact, Kumar et al. (2018a) suggest two alterations to the phase-field formulation (2), one pertaining to nucleation, the other to healing. In this paper, our focus is nucleation.

We then introduce a phase-field model that circumvents the shortcomings of the current phase-field approach while keeping undisturbed its ability to model crack propagation. We do so in Section 4. Following Kumar et al. (2018a), the central idea is to implicitly account for the presence of the inherent microscopic defects – whose macroscopic manifestation is the strength of the material – through the addition of an external driving force c_ε in the equation governing the evolution of the phase field v .

We conclude this work by showcasing in Section 5 the descriptive and predictive capabilities of the proposed phase-field model via sample simulations of experiments spanning a broad spectrum of materials and the full range of fracture nucleation settings and by recording a number of final comments in Section 6.

2. The basic ingredients for the modeling of fracture nucleation

Experimental results generated over decades indicate that macroscopic crack nucleation in homogeneous brittle materials falls into one of the three different types schematically depicted in Fig. 1; see, e.g., Irwin (1958), Usami et al. (1986), Bažant (2005), and references therein. The next three subsections outline the three different types, one at a time. Any attempt at a comprehensive macroscopic theory of fracture nucleation should convincingly handle all three.

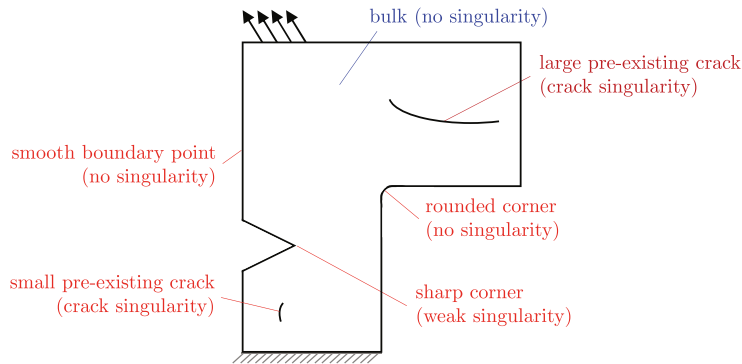


Fig. 1. Schematic of a structure made of a homogeneous brittle material under general quasistatic boundary conditions. Fracture may nucleate: i) at material points in the bulk, ii) from large pre-existing cracks, or iii) from the boundary, be it straight or be it a corner, or small pre-existing cracks. Fracture nucleation in the bulk is governed by the strength of the material. On the other hand, fracture nucleation from large pre-existing cracks – featuring what we call here a crack singularity – is governed by the Griffith competition between the material bulk elastic energy and surface fracture energy. Finally, fracture nucleation from straight boundaries or corners – featuring what we call here a weak singularity – and from small pre-existing cracks is governed by the interaction among all three properties of the material: its strength, its bulk elastic energy, and its surface fracture energy. Here, weak singularity means that around such a point the elastic energy density on a small ball decreases faster than the radius of the ball.

2.1. Nucleation in the bulk: The strength

Brittle materials contain inherent defects of mostly micron and submicron size; see, e.g., Tomsia and Glaeser (1998), Bradt et al. (2005), and Mark et al. (2013). When a specimen made of a brittle material is subjected to a state of monotonically increasing uniform stress, fracture will nucleate from one or more of those pre-existing defects at a finite critical value of the applied stress. The set of all such critical stresses defines a surface in stress space

$$\mathcal{F}(\sigma) = 0, \quad (3)$$

² See also Poulain et al. (2017), Poulain et al. (2018) who analyzed new experiments in the spirit of the classical ones but carried out at high spatiotemporal resolution.

Table 1

Material constants for titania (Ely, 1972; Iuga et al., 2007) and graphite (Goggin and Reynolds, 1967; Sato et al., 1987) used throughout this work.

	titania (TiO ₂)	graphite
shear modulus (μ)	97 GPa	4.3 GPa
bulk modulus (κ)	198 GPa	4.4 GPa
Young's modulus (E)	250 GPa	9.8 GPa
Poisson's ratio (ν)	0.29	0.13
tensile strength (σ_{ts})	100 MPa	27 MPa
compressive strength (σ_{cs})	1232 MPa	77 MPa
critical energy release rate (G_c)	36 N/m	91 N/m

which we refer to as the *strength surface* of the material. Experimental evidence points to the intrinsic character of such a surface.³ We posit henceforth that this surface is truly a material datum.

Of course, it is extremely difficult to carry out experiments that probe the entire 6-dimensional space of uniform stresses σ in space dimension $N = 3$. For materials whose elastic response is isotropic (the class of materials of interest in this work), it is reasonable to postulate that their strength surface is also isotropic; see, e.g., Chapter 10 in the monograph by Munz and Fett (1999). Then

$$\mathcal{F}(\sigma) = \tilde{\mathcal{F}}(\sigma_1, \sigma_2, \sigma_3) = \hat{\mathcal{F}}(I_1, J_2, J_3) = 0, \quad (4)$$

where $\sigma_1, \sigma_2, \sigma_3$ stand for the principal stresses and

$$I_1 = \text{tr } \sigma, \quad J_2 = \frac{1}{2} \text{tr } \sigma_D^2, \quad J_3 = \frac{1}{3} \text{tr } \sigma_D^3 \quad \text{with} \quad \sigma_D = \sigma - \frac{1}{3} (\text{tr } \sigma) \mathbf{I} \quad (5)$$

denote the standard invariants.⁴

The specific strength surface

$$\mathcal{F}(\sigma) = \sqrt{J_2} + \frac{\sigma_{cs} - \sigma_{ts}}{\sqrt{3}(\sigma_{cs} + \sigma_{ts})} I_1 - \frac{2\sigma_{cs}\sigma_{ts}}{\sqrt{3}(\sigma_{cs} + \sigma_{ts})} = 0 \quad (6)$$

is of particular interest for later reference. There, the material constants σ_{ts} and σ_{cs} stand for the tensile and compressive strengths of the material under uniaxial loading, say when $\sigma = \text{diag}(\sigma_1, 0, 0)$ with $\sigma_1 > 0$ and $\sigma_1 < 0$, respectively. The strength surface (6) is exactly the criterion originally introduced in Drucker and Prager (1952) to model the yielding of soils.

Fig. 2 shows the comparisons between the strength surface (6), with $\sigma_{ts} = 100$ MPa and $\sigma_{cs} = 1232$ MPa in part (a) and $\sigma_{ts} = 27$ MPa and $\sigma_{cs} = 77$ MPa in part (b), and the experimental data of Ely (1972) for titania (TiO₂) and of Sato et al. (1987) for graphite; for later reference, Table 1 lists the elastic, strength, and toughness material constants for these two ceramics. The results correspond roughly to the case when $\sigma_3 = 0$ and are plotted in the space of principal stresses (σ_1, σ_2). In addition to the good agreement between the simple formula (6) and the experiments, we remark that the compressive strength $\sigma_{cs} = 1232$ MPa ($\sigma_{cs} = 77$ MPa) and the shear strength⁵ $\sigma_{ss} = 100$ ($\sigma_{ss} = 26$ MPa) are, respectively, about 12 (3) and 1 (0.95) times larger than the tensile strength $\sigma_{ts} = 100$ MPa ($\sigma_{ts} = 27$ MPa) of titania (graphite). These are well within the range of typical ratios $\sigma_{cs}/\sigma_{ts} \in [2, 20]$ and $\sigma_{ss}/\sigma_{ts} \in [0.9, 1.2]$ for many brittle materials; see Chapter 10 in Munz and Fett (1999).

³ Stochasticity is also present although irrelevant at this juncture; see, however, Subsection 5.1 below.

⁴ Even in the isotropic context of focus here, the experimental generation of isotropic strength surfaces (4) is a challenging endeavor. Indeed, the strength surfaces (4) of even the most common brittle materials are not fully available in the literature.

⁵ In the context of Fig. 2 simple shear loading corresponds to the line $\sigma_2 = -\sigma_1$.

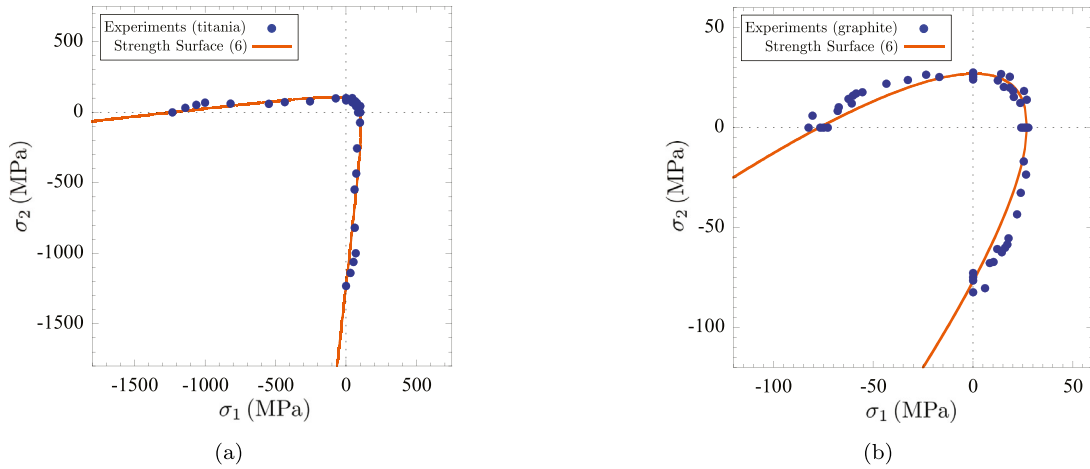


Fig. 2. Comparison between the Drucker-Prager strength surface (6) and the strength experimental data for: (a) titania due to Ely (1972) and (b) graphite due to Sato et al. (1987). The results are plotted for the principal stress σ_2 in terms of the principal stress σ_1 and correspond to the case when $\sigma_3 = 0$.

2.2. Nucleation from large pre-existing cracks: The critical energy release

When the domain under investigation already contains a large⁶ pre-existing crack, fracture may nucleate from the crack front. In other words, the crack may propagate. That the nucleation of fracture from large cracks in brittle materials is well described by the Griffith competition between bulk elastic energy and surface fracture energy is by now a settled matter. Roughly speaking, fracture may nucleate from a large pre-existing crack whenever the criterion

$$-\frac{\partial \mathcal{W}}{\partial \Gamma} = G_c$$

is satisfied, namely, whenever the change in potential energy \mathcal{W} in the structure with respect to an added surface area Γ to the crack reaches the critical elastic energy release rate G_c of the material. This falls squarely within the scope of the variational theory developed since Francfort and Marigo (1998).

The critical energy release rate G_c is often available in the literature. Further, standardized tests that measure G_c for a given material are readily carried out with conventional equipment; see, e.g., Chapter 6 in Zehnder (2012).

2.3. Nucleation from the boundary and small pre-existing cracks: The transition zone

We view the case of a crack nucleating from a boundary point or a small pre-existing crack as the result of a mediation between strength and energy release. An abundance of experimental results for the nucleation of fracture emanating from smooth and sharp corners and from small cracks can be found in the literature, and this within a wide range of brittle materials. Fig. 3 presents a set of representative experimental results for the nucleation of fracture in single-edge-notch specimens of alumina (Al_2O_3), with Young's modulus $E = 335$ GPa and Poisson's ratio $\nu = 0.25$, due to Kimoto et al. (1985); see also Usami et al. (1986). Specifically, the critical value of the applied stress at which fracture nucleates from the notch is plotted as a function of the depth of the notch. For notches smaller than 0.01 mm in depth, fracture nucleation is seen to be well described by the tensile strength of the material $\sigma_{ts} = 210$ MPa (dotted line in the figure). For notches larger than 0.2 mm, on the other hand, fracture nucleation is well described by the Griffith competition between elastic and surface fracture energy with critical energy release rate $G_c = 26.8$ N/m (dashed line in the figure⁷). The transition behavior (shaded in gray) occurs for depth notches ranging from 0.01 mm to 0.2 mm.

⁶ "Large" refers to large relative to the characteristic size of the inherent microscopic defects in the material under investigation. By the same token, "small" refers to sizes that are of the same order or just moderately larger than the sizes of the inherent defects.

⁷ The dashed line in Fig. 3 corresponds to the classical formula $\sigma_{cr}^{\text{LEFM}} = \cos(\pi a/2b) \sqrt{G_c E / \pi a} / ((0.752 + 2.02(a/b) + 0.37(1 - \sin(\pi a/2b))^3) \sqrt{2b/\pi \tan(\pi a/2b)})$, reported e.g. in Chapter 2 of the handbook by Tada et al. (1973), for the critical tensile stress at which a pre-existing single-edge crack of size a in a plate of width b and length $L \geq 3b$ propagates.

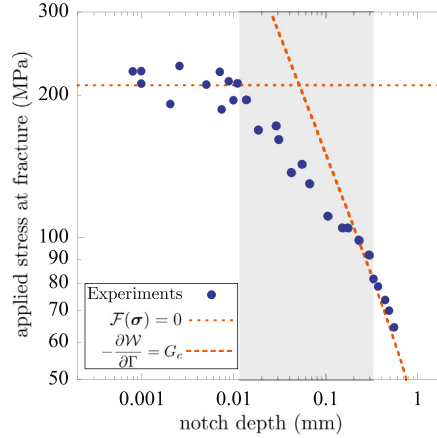


Fig. 3. Experimental data of Kimoto et al. (1985) for the critical stress at which fracture nucleates from the notch in single-edge-notch specimens made of alumina, plotted as a function of the depth of the notch.

3. Existing phase-field approaches to model fracture nucleation

As mentioned before, the phase-field approach to brittle fracture characterized by the family of minimization problems (2) provides a good description⁸ of fracture nucleation from large pre-existing cracks. However, the approach fails when fracture nucleation occurs in the bulk, from boundaries, or from small cracks. This is so because the minimization problem (2) – being a regularization of the Griffith energy competition (1) – does not incorporate any information about the strength of the material and predicts as a result that the critical applied load at which fracture nucleates from those sites will increase to infinity as the length $\varepsilon \searrow 0$, this for any choice of $\psi(v)$ and $s(v)$. A possible remedy takes aim at that pathology.

3.1. Imparting physical meaning to the localization length ε

Amor et al. (2009) recognized that a suitable fixed value of ε , identified as a material characteristic length, would result in the correct prediction of the nucleation of fracture in a bar under uniform uniaxial tension at the right tensile strength σ_{ts} . In their footsteps, numerous authors have advocated this approach; see, e.g., Pham et al. (2011), Borden et al. (2012), Mesgarnejad et al. (2015), Nguyen et al. (2016), Pham et al. (2017), Alessi et al. (2018), Tanné et al. (2018). The last reference has shown that such an approach does lead to good quantitative agreement with numerous experimental results – on many ceramics, metals, and hard polymers with similar Poisson's ratios $\nu \leq 0.36$ – for the nucleation of fracture from smooth and sharp boundary points in specimens that are subject to nominally tensile loads. In spite of this agreement, the approach is insufficient. Here is why.

i) The value of localization length ε that results from matching the tensile strength σ_{ts} of a given material may be extremely small or extremely large relative to the size of the structure. Both are problematic from a practical point of view.

As an example, recall from Tanné et al. (2018) that for the “classical choice” $\psi(v) = v^2$ and $s(v) = 1 - v$, the resulting localization length for a material with Young's modulus E , tensile strength σ_{ts} , and critical energy release rate G_c is given by

$$\varepsilon = \frac{3G_c E}{8\sigma_{ts}^2}. \quad (7)$$

In the case of the PMMA (polymethyl methacrylate) studied in Dunn et al. (1997), $E = 2300$ MPa, $\sigma_{ts} = 124$ MPa, and $G_c = 461$ N/m, and so it follows from (7) that $\varepsilon = 25 \times 10^{-6}$ m. Since any kind of finite element implementation of (2) requires meshes that are of $o(\varepsilon)$ -size, any large-size structure is beyond reach. On the other hand, for a mortar studied in Giaccio and Zerbino (1998), $E = 31.8$ GPa, $\sigma_{ts} = 3.6$ MPa, and $G_c = 55$ N/m, so that from (7) $\varepsilon = 0.05$ m. In this case, any small-size structure is beyond reach.

ii) Tying up the value of ε in (2) to the tensile strength σ_{ts} (or to any other single strength data point for that matter) of a given material of interest arbitrarily privileges a *single* point on the strength surface while ignoring the rest of that surface.

Take for example $\psi(v) = v^2$ and $s(v) = 1 - v$. For such a choice, we show in Appendix A that, under states of uniform (but otherwise arbitrary) stress σ , v will cease to be identically 1 and further that stability will be lost whenever the alge-

⁸ To be precise, the formulation (2) predicts critical stresses at nucleation from large pre-existing cracks that are consistently larger by at least ten percent than the corresponding exact solutions from LEFM. If the phase field is set to $v = 0$ around crack fronts, that discrepancy disappears; see, e.g., Tanné et al. (2018).

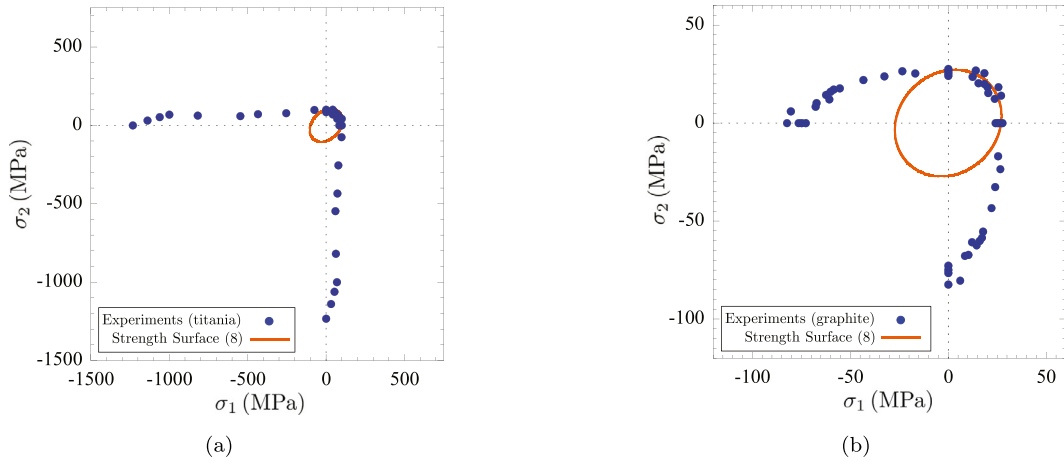


Fig. 4. Comparison between the strength surface (8) and the strength experimental data for titania and graphite displayed in Fig. 2.

braic equation

$$\mathcal{F}^{\sigma_{ts}}(\sigma) = \frac{J_2}{\mu} + \frac{I_1^2}{9\kappa} - \frac{\sigma_{ts}^2}{E} = 0 \quad (8)$$

is satisfied; recall that $\kappa = \lambda + 2\mu/3$ and $E = 9\mu\kappa/(\mu + 3\kappa)$ in dimension $N = 3$. We identify criterion (8) with fracture nucleation in the bulk because one can evidence numerically that localization of v near 0 immediately follows the loss of stability characterized by (8).

In other words, Eq. (8) defines the strength surface predicted by the phase-field model (2), for the case when $\psi(v) = v^2$, $s(v) = 1 - v$, and when the localization length is prescribed by (7). Fig. 4 compares this surface with the same strength experimental data of Ely (1972) and of Sato et al. (1987) displayed in Fig. 2 for titania and graphite with material constants listed in Table 1. While the strength surface (8) correctly predicts nucleation of fracture for uniaxial tensile stress when $\sigma_2 = 0$ ($\sigma_1 = 0$) and $\sigma_1 > 0$ ($\sigma_2 > 0$), it fails in most other stress states. For instance, under simple shear stress when $\sigma_2 = -\sigma_1$, it predicts fracture nucleation at 62 MPa (18 MPa) for the titania (graphite) material, but its shear strength is $\sigma_{ss} = 100$ MPa ($\sigma_{ss} = 26$ MPa). Further, under uniaxial compressive stress, it predicts fracture nucleation at 100 MPa (27 MPa), but the compressive strength of that titania (graphite) is $\sigma_{cs} = 1232$ MPa ($\sigma_{cs} = 77$ MPa).

iii) While the representative criterion (8) is written in terms of the stress invariants I_1 and J_2 , it is in truth an *energy criterion* and not a *stress criterion* of the type mandated by the strength surface (4). As such, it is intrinsically inadequate to model fracture nucleation in the bulk of brittle materials at macroscopic length scales.

The energetic character of the criterion (8) is readily seen by considering its behavior for increasingly larger ratios of bulk modulus κ to shear modulus μ , as done in Fig. 5 for $\kappa/\mu = 1, 10$, and 100. The results in part (a) of the figure are plotted in the space of normalized principal stresses ($\sigma_1/\sigma_{ts}, \sigma_2/\sigma_{ts}, \sigma_3/\sigma_{ts}$), while those in part (b) correspond to the cross section of stress states with $\sigma_3 = \sigma_2$. The immediate observation is that, for stress states with all principal stresses positive and large, the strength surface (8) predicts fracture nucleation at increasingly larger stresses for increasing κ/μ . This nonphysical behavior is nothing more than the manifestation of the fact that the elastic energy in increasingly incompressible materials can be arbitrarily small, while, at the same time, the hydrostatic stress can be arbitrarily large.

4. The proposed phase-field approach

Next, we proceed with the introduction of a phase-field model that should describe nucleation not only from large pre-existing cracks but also from small pre-existing cracks, smooth and non-smooth boundary points, as well as within the bulk. This should be accomplished without jeopardizing the predictive value of (2) for crack propagation.

We restrict the presentation to isotropic linear elastic brittle materials with stored-energy function

$$W(\mathbf{E}) = \mu \operatorname{tr} \mathbf{E}^2 + \left(\frac{\kappa}{2} - \frac{\mu}{3} \right) (\operatorname{tr} \mathbf{E})^2,$$

with $\mu > 0$ and $\kappa > 0$, a strength surface of the form

$$\mathcal{F}(\sigma) = \hat{\mathcal{F}}(I_1, J_2) = 0, \quad (9)$$

and constant critical energy release rate G_c , in $N = 3$ space dimensions.

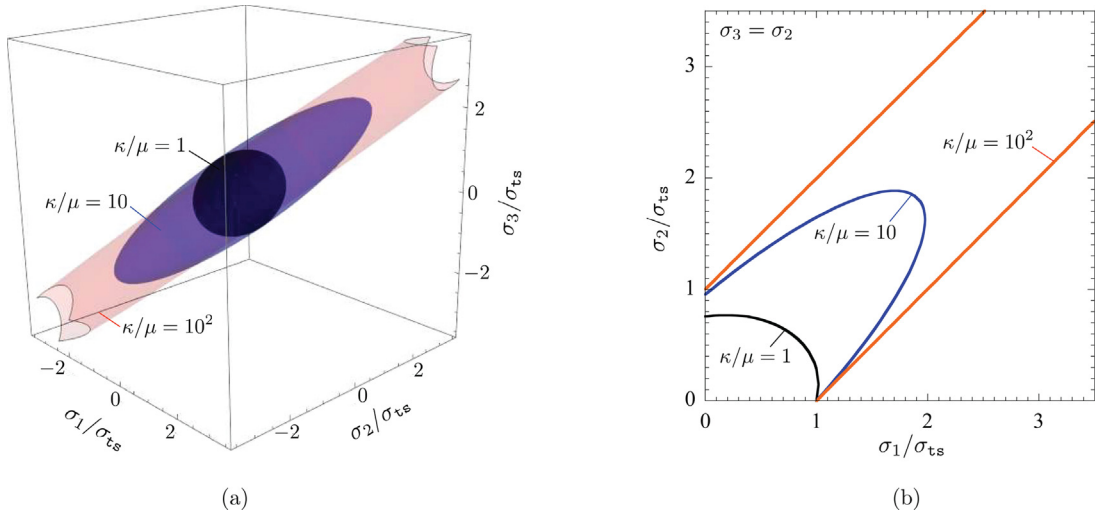


Fig. 5. (a) The strength surface (8) plotted in the space of normalized principal stresses $(\sigma_1/\sigma_{ts}, \sigma_2/\sigma_{ts}, \sigma_3/\sigma_{ts})$ for three increasing values of bulk-modulus-to-shear-modulus ratio: $\kappa/\mu = 1, 10$, and 100 . (b) The cross section of the same surface for stress states with $\sigma_3 = \sigma_2$.

4.1. The general model

Following Kumar et al. (2018a), we begin by considering the Euler-Lagrange equations associated with the variational problem (2) – and not the variational problem (2) itself – in the case where

$$\psi(v) = v^2 \quad \text{and} \quad s(v) = 1 - v. \quad (10)$$

We allow for both traction and body forces

$$\bar{\mathbf{t}}(\mathbf{x}, t), \quad (\mathbf{x}, t) \in \partial\Omega_N \times [0, T] \quad \text{and} \quad \mathbf{b}(\mathbf{x}, t), \quad (\mathbf{x}, t) \in \Omega \times [0, T]$$

in the Euler-Lagrange equation for the displacement field $\mathbf{u}(\mathbf{x}, t)$. More importantly, we also include an external driving force

$$c_e(\mathbf{x}, t), \quad (\mathbf{x}, t) \in \Omega \times [0, T]$$

in the Euler-Lagrange equation for the phase field $v(\mathbf{x}, t)$. The resulting governing equations for the displacement field $\mathbf{u}_k(\mathbf{x}) = \mathbf{u}(\mathbf{x}, t_k)$ and the phase field $v_k(\mathbf{x}) = v(\mathbf{x}, t_k)$ at any given discrete time $t_k \in \{0 = t_0, t_1, \dots, t_m, t_{m+1}, \dots, t_M = T\}$ read as

$$\begin{cases} \operatorname{div} \left[v_k^2 \frac{\partial W}{\partial \mathbf{E}}(\mathbf{E}(\mathbf{u}_k)) \right] + \mathbf{b}(\mathbf{x}, t_k) = \mathbf{0}, & \mathbf{x} \in \Omega, \\ \mathbf{u}_k = \bar{\mathbf{u}}(\mathbf{x}, t_k), & \mathbf{x} \in \partial\Omega_D, \\ \left[v_k^2 \frac{\partial W}{\partial \mathbf{E}}(\mathbf{E}(\mathbf{u}_k)) \right] \mathbf{n} = \bar{\mathbf{t}}(\mathbf{x}, t_k), & \mathbf{x} \in \partial\Omega_N \end{cases} \quad (11)$$

and

$$\begin{cases} \varepsilon G_c \Delta v_k = \frac{8}{3} v_k W(\mathbf{E}(\mathbf{u}_k)) - \frac{4}{3} c_e(\mathbf{x}, t_k) - \frac{G_c}{2\varepsilon}, & \text{if } v_k(\mathbf{x}) < v_{k-1}(\mathbf{x}), \quad \mathbf{x} \in \Omega \\ \varepsilon G_c \Delta v_k \geq \frac{8}{3} v_k W(\mathbf{E}(\mathbf{u}_k)) - \frac{4}{3} c_e(\mathbf{x}, t_k) - \frac{G_c}{2\varepsilon}, & \text{if } v_k(\mathbf{x}) = 1 \text{ or } v_k(\mathbf{x}) = v_{k-1}(\mathbf{x}) > 0, \quad \mathbf{x} \in \Omega \\ v_k(\mathbf{x}) = 0, & \text{if } v_{k-1}(\mathbf{x}) = 0, \quad \mathbf{x} \in \Omega \\ \nabla v_k \cdot \mathbf{n} = 0, & \mathbf{x} \in \partial\Omega \end{cases} \quad (12)$$

Further we set $\mathbf{u}(\mathbf{x}, 0) \equiv \mathbf{0}$ and $v(\mathbf{x}, 0) \equiv 1$.

Physically, the external driving force c_e in (12) can be thought of as the macroscopic manifestation of the presence of the inherent microscopic defects in the material. As elaborated in the next subsection, it is hence the quantity that allow us to incorporate its strength surface (9) into the model.

Remark 1. Much like in the original formulation (2), the localization length ε in Eqs. (11)–(12) is just a regularization parameter that is void of any further physical meaning. Accordingly, one should undertake the task of passing to the limit as

$\varepsilon \searrow 0$ in the system of Eqs. (11)–(12), showing that it converges in some reasonable topology to a putative set of “equations” that models both nucleation and propagation in brittle fracture. Although numerical evidence points to the existence of such a set of equations, for now, passing to the limit remains a formidable task. Just to mention one hurdle, no one even knows what equations, if any, one should write for crack propagation once the crack path is set free, that is, how to generalize the Griffith system of equations when cracks are free to choose their topology.

4.2. The proposed external driving force c_e

As alluded to earlier, the strength surface (9) of a given material of interest is at best partly known. Mostly, only the tensile strength σ_{ts} and compressive strength σ_{cs} are usually available in the literature. So in practice one must resort to the use of a model to extrapolate the available strength data to the entire stress space.

In this subsection, we describe how to construct an external driving force c_e in the phase-field model (11)–(12) for the case when the given strength surface (9) is of the Drucker-Prager type

$$\hat{\mathcal{F}}(I_1, J_2) = \sqrt{J_2} + \gamma_1 I_1 + \gamma_0 = 0, \quad (13)$$

where γ_0 and γ_1 stand for material constants, and note that the procedure for other types of strength surfaces would not be fundamentally different.

Remark 2. When the material constants γ_0 and γ_1 are calibrated with the tensile and compressive strengths, they read as

$$\gamma_1 = \frac{\sigma_{cs} - \sigma_{ts}}{\sqrt{3}(\sigma_{cs} + \sigma_{ts})} \quad \text{and} \quad \gamma_0 = -\frac{2\sigma_{cs}\sigma_{ts}}{\sqrt{3}(\sigma_{cs} + \sigma_{ts})}$$

and the Drucker-Prager strength surface (13) takes the conventional form (6).

Considering the form of the strength surface (13), we begin by restricting attention to external driving forces c_e that are only functions of the first (5)₁ and second (5)₂ invariants of the stress associated with the degradation function in (10), that is of $\sigma(\mathbf{x}, t) = \nu^2 \frac{\partial W}{\partial \mathbf{E}}(\mathbf{E})$, as well as of the localization length ε . We thus write

$$c_e = \hat{c}_e(I_1, J_2; \varepsilon). \quad (14)$$

Note that the expressions for the invariants in (14) are given in terms of the displacement field \mathbf{u} and phase field v by

$$I_1 = 3\kappa\nu^2 \text{tr} \mathbf{E} \quad \text{and} \quad J_2 = 2\mu^2\nu^4 \text{tr} \mathbf{E}_D^2 \quad \text{with} \quad \mathbf{E}_D = \mathbf{E} - \frac{1}{3}(\text{tr} \mathbf{E})\mathbf{I},$$

where we recall that $\mathbf{E} = 1/2(\nabla \mathbf{u} + \nabla \mathbf{u}^T)$.

Even though we have not determined the limit as $\varepsilon \searrow 0$ of the governing Eqs. (11)–(12), numerical experiments suggest that in order to being able to do so we must heed two guiding principles in the construction of external driving forces within the class (14). Precisely, they should:

1. have identical functional form as the given strength surface but with ε -dependent coefficients that are suitably picked so that, in the limit as the localization length $\varepsilon \searrow 0$, the resulting phase-field model (11)–(12) predicts fracture nucleation in the bulk exactly according to the given strength surface, and
2. allow for possibly non-zero values $\hat{c}_e(0, 0; \varepsilon) \neq 0$ in the ground state when $I_1 = J_2 = 0$ so that the resulting phase-field model (11)–(12) predicts nucleation and propagation of fracture from large cracks according to the critical energy release rate G_c .

In view of the above, we propose

$$\hat{c}_e(I_1, J_2; \varepsilon) = \frac{1}{1 + \beta_3^\varepsilon I_1^2} \left(\beta_2^\varepsilon \sqrt{J_2} + \beta_1^\varepsilon I_1 + \beta_0^\varepsilon \right) \quad (15)$$

with

$$\begin{cases} \beta_0^\varepsilon = \delta^\varepsilon \frac{3G_c}{8\varepsilon} \\ \beta_1^\varepsilon = \left(\frac{(1 + \delta^\varepsilon)\gamma_1}{\gamma_0} \right) \frac{3G_c}{8\varepsilon} \\ \beta_2^\varepsilon = \left(\frac{1 + \delta^\varepsilon}{\gamma_0} \right) \frac{3G_c}{8\varepsilon} \\ \beta_3^\varepsilon = \alpha\varepsilon \end{cases}, \quad (16)$$

where δ^ε is a unitless ε -dependent coefficient while α is a - non-negative parameter with unit $\text{length}^3/\text{force}^2$.

Remark 3. As elaborated further below, the selection of the coefficient δ^ε is critical for the resulting phase-field model to correctly predict fracture nucleation from large pre-existing cracks according to the Griffith competition between the elastic and surface energies. On the other hand, based on a wide range of numerical experiments (not shown here), the specific choice for the parameter α is of little consequence, so long as it is non-negative and does not lead to numerical instabilities. In all that follows, we set $\alpha = \sigma_{ts}/(\mu\kappa G_c)$ so that

$$\beta_3^\varepsilon = \left(\frac{\sigma_{ts}}{\mu\kappa}\right) \frac{1}{G_c}. \quad (17)$$

The coefficient (17) has the benefit of resulting in an external driving force (15) that vanishes at crack and weak singularities. At this point, it is not entirely clear whether such a feature is necessary to being able to pass to the limit as $\varepsilon \searrow 0$ or the simpler choice $\alpha = 0$ and hence $\beta_3^\varepsilon = 0$ suffices.

Now, the value of the localization length ε is always finite in practice. It is thus desirable to generalize the external driving force (15)–(16) so that the resulting phase-field model be capable of predicting the nucleation and propagation of fracture accurately not only asymptotically in the limit as $\varepsilon \searrow 0$ but also at finite values of ε . This can be accomplished by adding corrections of $O(\varepsilon^0)$ and higher orders in ε to the coefficients β_1^ε and β_2^ε in (16). The algebra involved in the addition of such corrections favors the use of strength material constants in (13) that have direct physical meaning, as opposed to the generic constants γ_0 and γ_1 (see comments around Fig. 6 below). For definiteness, we shall use here the tensile strength σ_{ts} and the compressive strength σ_{cs} . The corresponding coefficients turn out to be given by

$$\begin{aligned} \beta_1^\varepsilon &= -\left(\frac{(1+\delta^\varepsilon)(\sigma_{cs}-\sigma_{ts})}{2\sigma_{cs}\sigma_{ts}}\right) \frac{3G_c}{8\varepsilon} - \frac{(8\mu+24\kappa-27\sigma_{ts})(\sigma_{cs}-\sigma_{ts})}{144\mu\kappa} - \left(\frac{(\mu+3\kappa)(\sigma_{cs}^3-\sigma_{ts}^3)\sigma_{ts}}{18\mu^2\kappa^2}\right) \frac{\varepsilon}{G_c}, \\ \beta_2^\varepsilon &= -\left(\frac{\sqrt{3}(1+\delta^\varepsilon)(\sigma_{cs}+\sigma_{ts})}{2\sigma_{cs}\sigma_{ts}}\right) \frac{3G_c}{8\varepsilon} - \frac{(8\mu+24\kappa-27\sigma_{ts})(\sigma_{cs}+\sigma_{ts})}{48\sqrt{3}\mu\kappa} - \left(\frac{(\mu+3\kappa)(\sigma_{cs}^3+\sigma_{ts}^3)\sigma_{ts}}{6\sqrt{3}\mu^2\kappa^2}\right) \frac{\varepsilon}{G_c}. \end{aligned} \quad (18)$$

Substitution of the coefficients (16)₁, (17), and (18) in expression (15) yields the final form of the proposed external driving force:

$$\begin{aligned} \widehat{c}_\varepsilon(I_1, J_2; \varepsilon) &= \frac{1}{1 + \frac{\varepsilon\sigma_{ts}}{\mu\kappa G_c} I_1^2} \left[\left(-\frac{3\sqrt{3}(\sigma_{cs}+\sigma_{ts})(1+\delta^\varepsilon)G_c}{16\sigma_{cs}\sigma_{ts}\varepsilon} + \frac{8\mu+24\kappa-27\sigma_{ts}}{48\sqrt{3}\mu\kappa} (\sigma_{cs}+\sigma_{ts}) + \right. \right. \\ &\quad \left. \left. \frac{\mu+3\kappa}{6\sqrt{3}\mu^2\kappa^2 G_c} \sigma_{ts}(\sigma_{cs}^3+\sigma_{ts}^3)\varepsilon \right) \sqrt{J_2} + \left(-\frac{3(\sigma_{cs}-\sigma_{ts})(1+\delta^\varepsilon)G_c}{16\sigma_{cs}\sigma_{ts}\varepsilon} - \right. \right. \\ &\quad \left. \left. \frac{8\mu+24\kappa-27\sigma_{ts}}{144\mu\kappa} (\sigma_{cs}-\sigma_{ts}) - \frac{\mu+3\kappa}{18\mu^2\kappa^2 G_c} \sigma_{ts}(\sigma_{cs}^3-\sigma_{ts}^3)\varepsilon \right) I_1 + \delta^\varepsilon \frac{3G_c}{8\varepsilon} \right]. \end{aligned} \quad (19)$$

We remark that this expression depends directly on the elastic constants μ , κ , the strength constants σ_{ts} , σ_{cs} , and the critical energy release rate G_c of the material of interest, as well as on the localization length ε . We also remark that it is a fully explicit expression up to the prescription of the coefficient δ^ε , whose calibration is detailed below in Subsection 4.3.2.

4.3. Properties of the proposed phase-field model

4.3.1. Nucleation in the bulk

Under states of uniform σ , the phase-field model (11)–(12) with an external driving force of the form (14) predicts that the phase field v ceases to be identically 1 whenever the algebraic equation

$$\widehat{\mathcal{F}}^\varepsilon(I_1, J_2) = \frac{J_2}{\mu} + \frac{I_1^2}{9\kappa} - \widehat{c}_\varepsilon(I_1, J_2; \varepsilon) - \frac{3G_c}{8\varepsilon} = 0 \quad (20)$$

is satisfied; see Appendix B for the derivation. Numerical experiments for several functions $\widehat{c}_\varepsilon(I_1, J_2; \varepsilon)$ suggest that localization of v near 0 always follows immediately after $v < 1$ for sufficiently small values of ε relative to the size of the structure. The condition (20) thus defines the strength surface predicted by the phase-field model.

Assuming rather generally that the asymptotic behavior of the coefficient δ^ε is taken to be of the form $\delta^\varepsilon = \delta_0\varepsilon^{-r} + \delta_1\varepsilon^{-r+1} + \delta_2\varepsilon^{-r+2} + \dots$ for some $r > 0$, it is not difficult to establish that the strength surface (20) predicted by the phase-field model (11)–(12) with external driving force (19) reduces asymptotically to

$$\widehat{\mathcal{F}}^\varepsilon(I_1, J_2) = \sum_{j=0}^{r-1} \delta_j \varepsilon^{-r-1+j} f_j(I_1) \left(\sqrt{J_2} + \frac{\sigma_{cs}-\sigma_{ts}}{\sqrt{3}(\sigma_{cs}+\sigma_{ts})} I_1 - \frac{2\sigma_{cs}\sigma_{ts}}{\sqrt{3}(\sigma_{cs}+\sigma_{ts})} \right) + O(\varepsilon^0) = 0$$

in the limit as the localization length $\varepsilon \searrow 0$, where $f_j(I_1)$ are known functions of I_1 (not spelled out here). That is, the predicted strength surface (20) with the external driving force (19) agrees identically – in an asymptotic sense – with the material strength surface (13), this for any choice of the coefficient δ^ε .

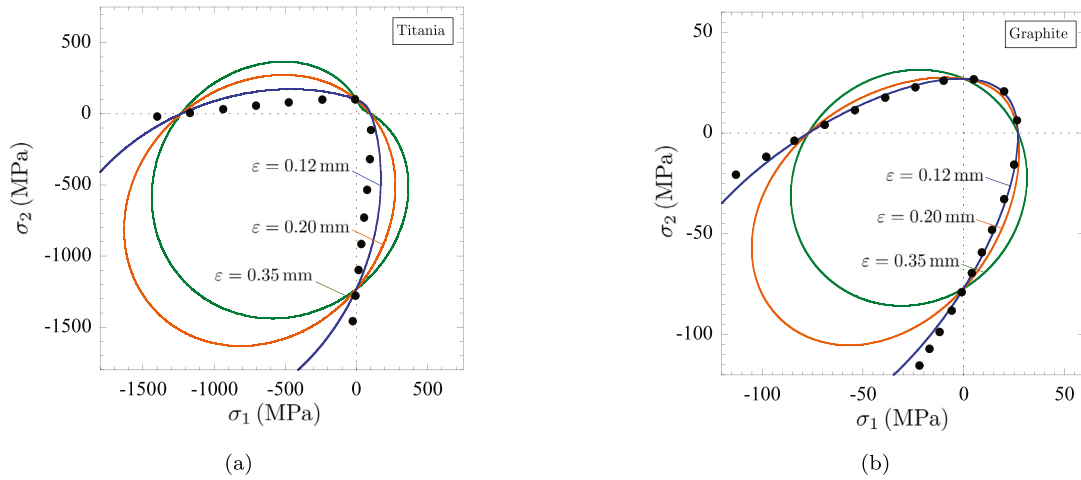


Fig. 6. Comparisons of the strength surface (20) predicted by the phase-field model (11)–(12) with external driving force (19) and the Drucker-Prager strength surface (6) for (a) titania and (b) graphite. The results are plotted for three decreasing values of the localization length ε in the principal stress space (σ_1, σ_2) for the case when $\sigma_3 = 0$.

Because of the higher order corrections that we added in (18) the predicted strength surface (20) agrees identically with the material strength surface (13) along uniaxial tension and compression loadings for arbitrary finite values of ε . This can be readily checked by substituting the external driving force (19) in (20) and evaluating the resulting strength surface along uniaxial tension (when $I_1 = \sigma_{ts}$, $J_2 = \sigma_{ts}^2/3$) and uniaxial compression (when $I_1 = -\sigma_{cs}$, $J_2 = \sigma_{cs}^2/3$). For other loading conditions, (20) provides an approximation for (13).

For illustration purposes, Fig. 6 presents results (solid lines) for the strength surface (20) predicted by the phase-field model (11)–(12) with the external driving force (19) for the same titania and graphite materials discussed in the two preceding sections. The results pertain to stress states with $\sigma_3 = 0$ and are plotted in the space of principal stresses (σ_1, σ_2) for the three values of localization length $\varepsilon = 0.35, 0.20$, and 0.12 mm and the corresponding coefficients $\delta^\varepsilon = 4.41, 6.27, 11.73$ for titania and $\delta^\varepsilon = 1.16, 3.22, 9.66$ for graphite (see Subsection 4.3.2 below for the calibration of these coefficients). As expected, the strength surface predicted by the proposed phase-field model converges to the given material strength surface (solid circles) as ε decreases.

In the context of nucleation of fracture in the bulk of a material, a relevant boundary-value problem is that of the nucleation of a single crack in a long prismatic bar under uniaxial tension. For such a problem, it is not difficult to work out an explicit solution of the governing equation (12) with external driving force (19) for the phase field v at the point at which the bar is severed into two pieces, say at $t = T$. Taking the bar to have cross-sectional area A and to occupy the domain $\Omega = [0, L] \times A$ aligned in the \mathbf{e}_1 direction of the laboratory frame of reference $\{\mathbf{e}_1, \mathbf{e}_2, \mathbf{e}_3\}$, the solution reads as

$$v(\mathbf{x}, T) = \begin{cases} 1 & \text{if } 0 \leq x_1 \leq x_1^0 - 2\varepsilon^* \\ 1 - \left(1 - \frac{|x_1 - x_1^0|}{2\varepsilon^*}\right)^2 & \text{if } x_1^0 - 2\varepsilon^* < x_1 < x_1^0 + 2\varepsilon^* \\ 1 & \text{if } x_1^0 + 2\varepsilon^* \leq x_1 \leq L \end{cases} \quad \text{with} \quad \varepsilon^* = \frac{\varepsilon}{\sqrt{1 + \delta^\varepsilon}}, \quad (21)$$

where x_1^0 denotes the location of the crack along the bar. Fig. 7 provides an schematic of this solution.

For the special case when $\delta^\varepsilon = 0$, it follows that $\varepsilon^* = \varepsilon$ and the solution (21) reduces identically to that found for the standard phase-field model (2) with the “classical choice” of degradation and surface localization functions (10); cf. Eq. (72) in Pham et al. (2011). For $\delta^\varepsilon > 0$ ($-1 < \delta^\varepsilon < 0$), on the other hand, the solution (21) is still of the same form as that found for the standard phase-field model but with an effectively smaller (larger) localization length $\varepsilon^* < \varepsilon$ ($\varepsilon^* > \varepsilon$). As elaborated next, properly calibrated values of δ^ε are not only positive but turn out to grow unbounded as $\varepsilon \searrow 0$. This implies that the actual localization length of the phase field v predicted by the phase-field model (11)–(12) with external driving force (19) is not of $O(\varepsilon)$ but of the smaller $O(\varepsilon^*)$. From a computational point of view, this implies that the use of moderately small values of ε generates results for which the localization length of the cracks (modeled by the phase field v) resemble sharp cracks. For instance, the values $\varepsilon = 0.35, 0.20, 0.12$ mm used in Fig. 6 correspond to localization lengths $\varepsilon^* = 0.150, 0.074, 0.034$ mm for titania and $\varepsilon^* = 0.238, 0.097, 0.037$ mm for graphite.

Remark 4. In order for the numerical solution of the governing equations (11)–(12) to be able to reproduce the “optimal” profile (21), the irreversibility constraint on the phase-field variable v has to be relaxed. This is because the length scale of the fronts of propagating cracks is ε and not ε^* , regardless of the value of δ^ε . Fig. 10(b) below shows an example of a propagating crack that illustrates this difference in sizes between the crack front and the crack profile. Accordingly, instead

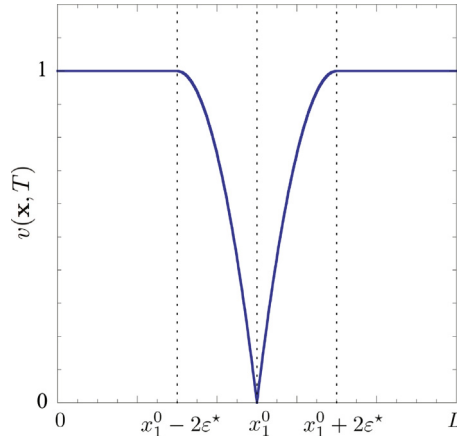


Fig. 7. Schematic of the phase-field solution (21) for the case when a single crack nucleates at x_1^0 in the bulk of a long bar of length L subject to uniaxial tension.

of requiring that v be non-increasing in time, we require that v be only non-increasing in time once it has reached a sufficiently small value, say v_i . In practice, it suffices to set $v_i \leq 0.05$.

4.3.2. Nucleation from large pre-existing cracks: The selection of the coefficient δ^ε

So far we have established that the phase-field model (11)–(12) with external driving force (19) predicts fracture nucleation in the bulk according to the strength surface (13) of the given material, this for sufficiently small localization lengths ε and any choice (within a very large class) of the coefficient δ^ε . As alluded to above, it turns out that the value of δ^ε does affect the occurrence of nucleation from large pre-existing cracks and hence must be calibrated accordingly.

In order to determine the correct value of δ^ε for a given set of material constants μ , κ , σ_{ts} , σ_{cs} , G_c and a given finite localization length ε , we consider a boundary-value problem for which the nucleation from a large pre-existing crack can be determined exactly – according to Griffith’s sharp theory of brittle fracture for linear elastic materials (LEFM) – and then have the phase-field model (11)–(12) with external driving force (19) match that exact solution thereby determining δ^ε .

We choose here the classical problem of a pre-existing crack of size $2a$ embedded at the center of a plate of width $2b$ and height $2L \geq 2b$ subject to a tensile force perpendicular to the crack. A simple exact asymptotic solution is available for this problem in the limit as $b \rightarrow \infty$. For finite b , Tada et al. (1973) reported the following approximate analytical solution (that differs from an exact power-series solution at most by 0.1%) for the critical applied stress $\sigma_{cr}^{\text{LEFM}}$ at which fracture nucleation occurs from the front of the pre-existing crack under plane-stress conditions:

$$\sigma_{cr}^{\text{LEFM}} = \frac{\sqrt{\cos\left(\frac{\pi a}{2b}\right)}}{1 - 0.025\left(\frac{a}{b}\right)^2 + 0.06\left(\frac{a}{b}\right)^4} \sqrt{\frac{G_c E}{\pi a}}, \quad (22)$$

where we recall that $E = 9\mu\kappa/(\mu + 3\kappa)$.

By way of an example, Fig. 8 presents the calibrated values of the coefficient δ^ε for the same titania and graphite materials referred to in Fig. 6. The results pertain to calculations on a plate with pre-existing crack size $2a = 40$ mm, width $b = 100$ mm, and height $2L = 600$ mm. Such a choice of the geometrical quantities guarantees that fracture nucleation occurs from the crack front and that it is governed by the critical energy release rate G_c . The finite-element method was utilized to solve numerically the appropriate plane-stress specialization of equations (11)–(12) with (19). Specifically, the results were generated by making use of a uniform and unstructured space discretization based on 3-node triangular elements featuring an average diameter $h = \varepsilon/10$ and linear approximations for both the displacement and the phase fields.

Remark 5. The above-described calibration process for the coefficient δ^ε should be carried out under the condition that $v = 0$ around the front of the pre-existing crack; Tanné et al. (2018) have referred to such a prescription as “damaged notch conditions”.

Remark 6. The results presented in Fig. 8, together with analogous results for other materials not included here, seem to hint at a δ^ε of the form $\delta^\varepsilon = \delta_0 \varepsilon^{-r} + o(\varepsilon^{-r+1})$ with $1 < r < 3$ in the limit as $\varepsilon \searrow 0$.

Remark 7. Because of the lack of an explicit approach for its calibration, it is not entirely clear whether an appropriate value of the coefficient δ^ε can always be found for a given material and choice of localization length ε . Numerical experiments suggest that δ^ε can always be appropriately calibrated for sufficiently small values of ε . The same does not appear to be true for large values of ε . In other words, the external driving force (19) does not resolve the practical issue of dealing with large structures.

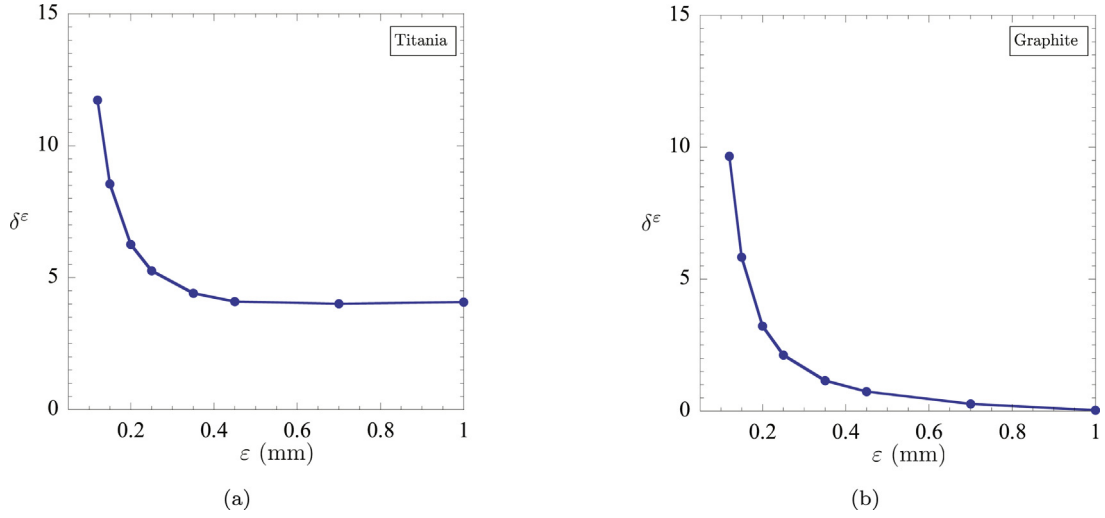


Fig. 8. The coefficient δ^ε determined by matching the predictions generated by the phase-field model (11)–(12) with external driving force (19) to the reference solution (22). The results are shown in terms of the localization length ε for (a) titania and (b) graphite.

4.3.3. Nucleation from the boundary and small pre-existing cracks

We now propose to check that the phase-field model (11)–(12) with external driving force (19) provides a proper mediation between fracture nucleation in the bulk and from large pre-existing cracks. We claim that it can thus describe fracture nucleation from boundary points and small pre-existing cracks without any further calibration. This we illustrate below by means of an example.

Fig. 9 presents results generated by the phase-field model for the critical stress σ_{cr} at which fracture nucleates from a pre-existing crack of size $2a \in [0.1, 40]$ mm, embedded at the center of a plate of width $2b = 200$ mm and height $2L = 200$ mm that is subjected to a tensile force perpendicular to the crack. The results are shown as functions of the crack size a and, in complete analogy with the preceding results, pertain to titania and graphite and the three values of localization length $\varepsilon = 0.35, 0.20$, and 0.12 mm.

Two observations are in order. The proposed phase-field model captures correctly – in a qualitative sense – the transition from the strength-dominated fracture (in these examples, $a < 0.1$ mm) to the critical-energy-release-rate-dominated fracture (in these examples, $a > 2$ mm) for both titania and graphite. Furthermore, the phase-field solutions for different values of the localization length ε are qualitatively and quantitatively very similar to one another and appear to converge as ε decreases.

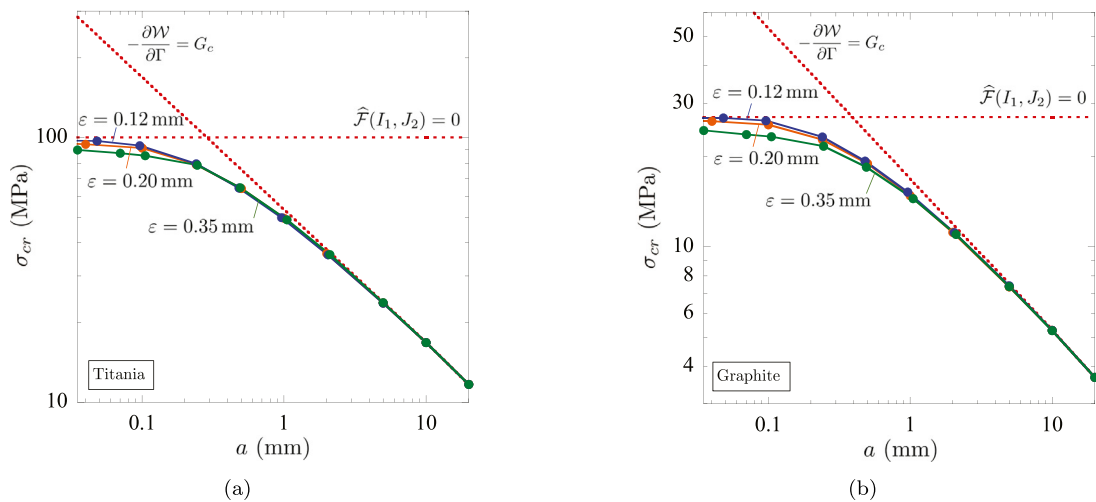


Fig. 9. Solutions generated by the phase-field model (11)–(12) with external driving force (19) for the critical stress σ_{cr} at which fracture nucleates from a pre-existing crack of size $2a$ embedded in a plate of width $2b = 200$ mm and height $2L = 200$ mm under tension. The results are shown for (a) titania and (b) graphite as functions of the crack size a for three decreasing values of the localization length ε . For direct comparison, the limiting results for fracture nucleation occurring based on the strength criterion ($\hat{\mathcal{F}}(I_1, J_2) = 0$) and on the critical energy release rate criterion ($-\partial\mathcal{W}/\partial\Gamma = G_c$, as characterized by the LEFM solution (22)) are also included.

4.3.4. Crack propagation

The three preceding subsections have established that the presence of the external driving force (19), with a properly calibrated value of δ^ε , in the governing equations (11)–(12) results in a phase-field model that captures the nucleation of fracture in the bulk, from large pre-existing cracks, as well as from boundary points and small pre-existing cracks. Next, we show that the presence of such an external driving force does not interfere with the propagation of fracture in the sense that the proposed phase-field model (11)–(12) predicts the same crack propagation as the standard phase-field model (2), and hence the same crack propagation as that dictated by the Griffith competition between bulk elastic energy and surface fracture energy.

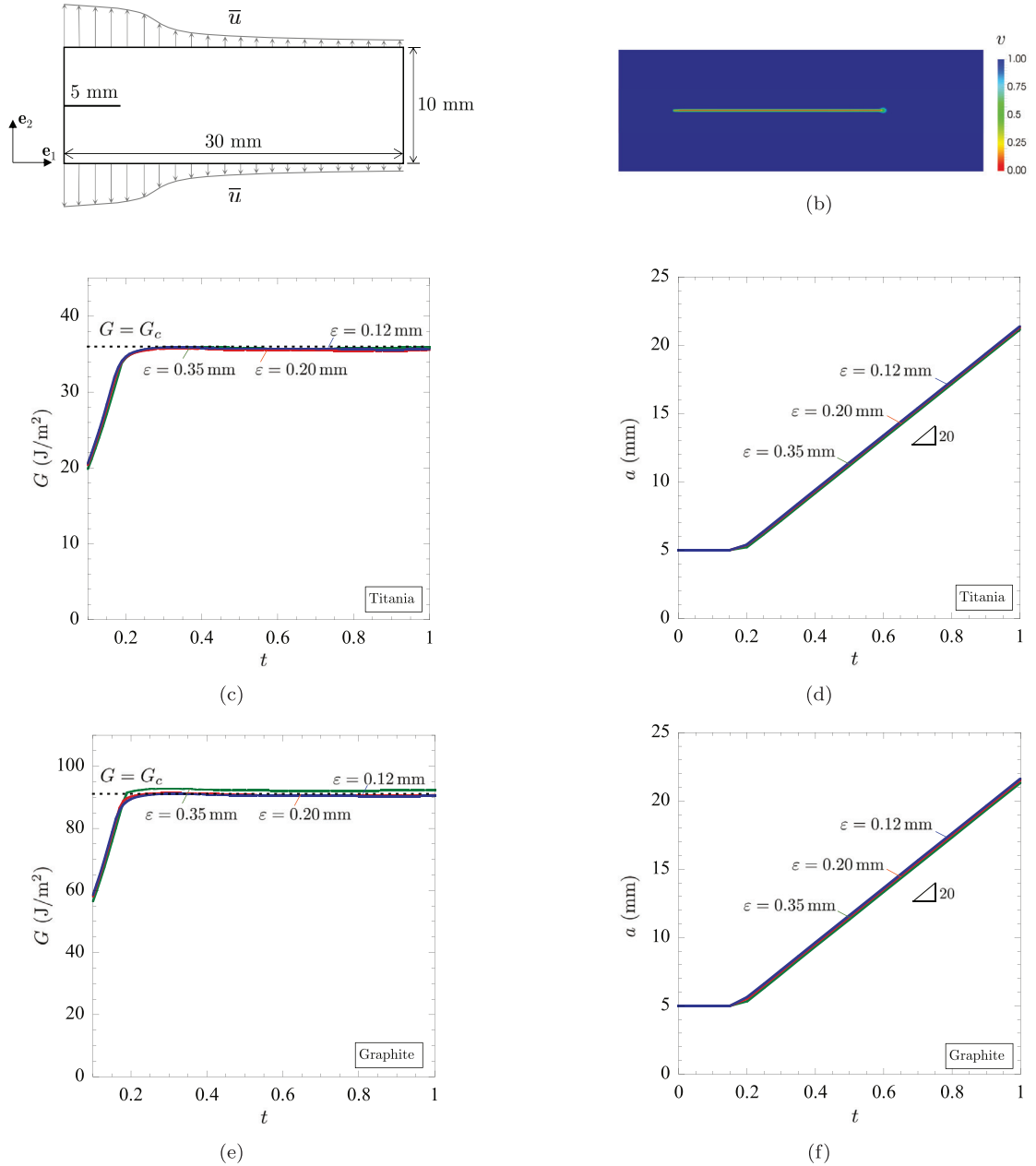


Fig. 10. Propagation of a crack along a straight path in strips of (c)–(d) titania and (e)–(f) graphite subject to the “surfing” boundary condition (23)–(24) schematically depicted in (a), as predicted by the phase-field model (11)–(12) with external driving force (19). (c)–(e) The energy release rate G as a function of time t for three decreasing values of the localization length ε . (d)–(f) The corresponding crack length a as a function of time t . (b) Contour plot of the phase field v at time $t = 1$ for the simulation on graphite with localization length $\varepsilon = 0.20$ mm.

To this effect, we consider the “surfing” boundary-value problem introduced by Hossain et al. (2014). The basic idea consists in subjecting a long strip of the material of interest with a pre-existing crack on its side to a suitably selected boundary condition that makes the pre-existing crack propagate at a prescribed “velocity” V . Consider hence a strip of 30 mm width and 10 mm height embedding an edge crack of initial size $a = 5$ mm along its centerline in the \mathbf{e}_1 direction, as schematically depicted in Fig. 10(a). In order to make the crack propagate at a prescribed “velocity” V , we subject the top ($x_2 = 5$ mm) and bottom ($x_2 = -5$ mm) boundaries of the strip to the displacement

$$\bar{u}_2(\mathbf{x}, t) = \bar{u}(x_1 - Vt, x_2) \quad (23)$$

within the setting of plane stress, where the particular form of the function \bar{u} is not critically important. Here, for definiteness, we make use of

$$\bar{u}(x_1, x_2) = \frac{(1+\nu)\sqrt{G_c}}{\sqrt{2\pi E}} [x_1^2 + x_2^2]^{1/4} \left[\frac{3-\nu}{1+\nu} - \cos\left(\tan^{-1}\left(\frac{x_2}{x_1}\right)\right) \right] \sin\left(\frac{1}{2} \tan^{-1}\left(\frac{x_2}{x_1}\right)\right), \quad (24)$$

which is one of the forms utilized by Hossain et al. (2014).

Fig. 10 shows predictions by the proposed phase-field model for the crack propagation in strips made of the same titania and graphite previously considered. We choose the “velocity” $V = 20$ mm in the applied displacement (23) with (24). The results also pertain to the same three decreasing values of the localization length considered above, $\varepsilon = 0.35, 0.20$, and 0.12 mm. Specifically, Figs. 10(c) and (e) report the evolution of the energy release rate G in the strips, obtained by calculating the J -integral over the boundary of the strips, while Figs. 10(d) and (f) show the associated crack length a , both as functions of the time t parameterizing the applied load. For completeness, Fig. 10(b) shows a contour plot of the phase field v at $t = 1$, when the crack has grown to a length of $a = 21.5$ mm, for the simulation on graphite with localization length $\varepsilon = 0.20$ mm for which, again, $\delta^\varepsilon = 3.22$ and $\varepsilon^* = 0.097$ mm.

The two main observations from Figs. 10(d) and (f) are that the pre-existing cracks start propagating at about $t = 0.18$ and that by around $t = 0.22$ subsequent loading results in their “steady-state” propagation at the prescribed constant “velocity” $V = 20$ mm, this irrespectively of the value of the localization length ε . The main observation from Figs. 10(c) and (e) is that the “steady-state” propagation of the cracks for $t > 0.22$ is associated with a constant value of the energy release rate G that is roughly equal to the critical energy release rate G_c . More specifically, all three localization lengths ε deliver values of G that are within 2% of G_c to which they appear to converge as ε decreases, indicating that the phase-field model (11)–(12) with external driving force (19), and a properly calibrated value of δ^ε , can predict crack propagation as dictated by Griffith's criterion.

5. Sample simulations and comparisons with experiments

In this final section, we illustrate via sample simulations the capabilities of the proposed phase-field model (11)–(12) with external driving force (19) to describe fracture nucleation in all possible settings: the bulk, large pre-existing cracks, boundary points, and small pre-existing cracks. With the dual objective of also providing insight into the predictive capabilities of the proposed model, the selected sample corresponds to simulations of experiments due to Sato et al. (1987), Cristiano et al. (2010), Pham et al. (2017), Gomez et al. (2009), and Kimoto et al. (1985) on a broad spectrum of materials. Precisely, Subsection 5.1 presents results for the nucleation of fracture within the bulk of graphite and PU (polyurethane) under multiaxial stress states. Subsection 5.2 presents results for the nucleation of fracture from a large pre-existing crack in PMMA under mixed-mode I + II loading. Finally, Subsection 5.3 presents results for the nucleation of fracture from a boundary point (in particular, a sharp corner) in a specimen made of PMMA and from a small pre-existing crack in single-edge-notch alumina specimens.

5.1. Nucleation in the bulk: Experiments on graphite and PU

We begin by demonstrating the capability of the proposed phase-field model to describe and predict fracture nucleation in the bulk by means of comparisons with the experiments of Sato et al. (1987) on graphite tubes and of Cristiano et al. (2010) on a PU poker-chip-type specimen.

The experiments on graphite. Sato et al. (1987) carried out experiments on tubes of inner radius $r_i = 10$ mm, outer radius $r_o = 15$ mm, and length $l = 90$ mm that were subjected to a combination of axial force P_A and inner pressure p_i , as schematically depicted in Fig. 11(a). The practical interest in this type of experiments is that it allows to access a wide range of quasi-uniform states of stress throughout the material making up the tube and hence can be effectively utilized to measure part of its strength surface.⁹

⁹ Prior to the nucleation of fracture, the elastic fields in the tube are available explicitly, in particular, as a function of the radial position r measured from the centerline of the tube, the principal stresses simply read as $\sigma_1 = \sigma_A = \frac{P_A}{\pi(r_o^2 - r_i^2)}$, $\sigma_2(r) = \frac{r_i^2 r_o^2 (p_i - p_o)}{(r_o^2 - r_i^2)r^2} + \frac{r_i^2 p_i - r_o^2 p_o}{r_o^2 - r_i^2}$, $\sigma_3(r) = -\frac{r_i^2 r_o^2 (p_i - p_o)}{(r_o^2 - r_i^2)r^2} + \frac{r_i^2 p_i - r_o^2 p_o}{r_o^2 - r_i^2}$, where p_o stands for the pressure on the outer surface of the tube; in the case of Sato et al. (1987), $p_o = 1$ atm = 0.1 MPa. For tubes of small thickness $\delta = r_o - r_i \ll r_o$, it follows from the above expressions that the stress in the material is asymptotically biaxial ($\sigma_3(r) = 0 + O(\delta^0)$) and uniform ($\sigma_2(r) = r_i(p_i - p_o)/\delta + O(\delta^0)$).

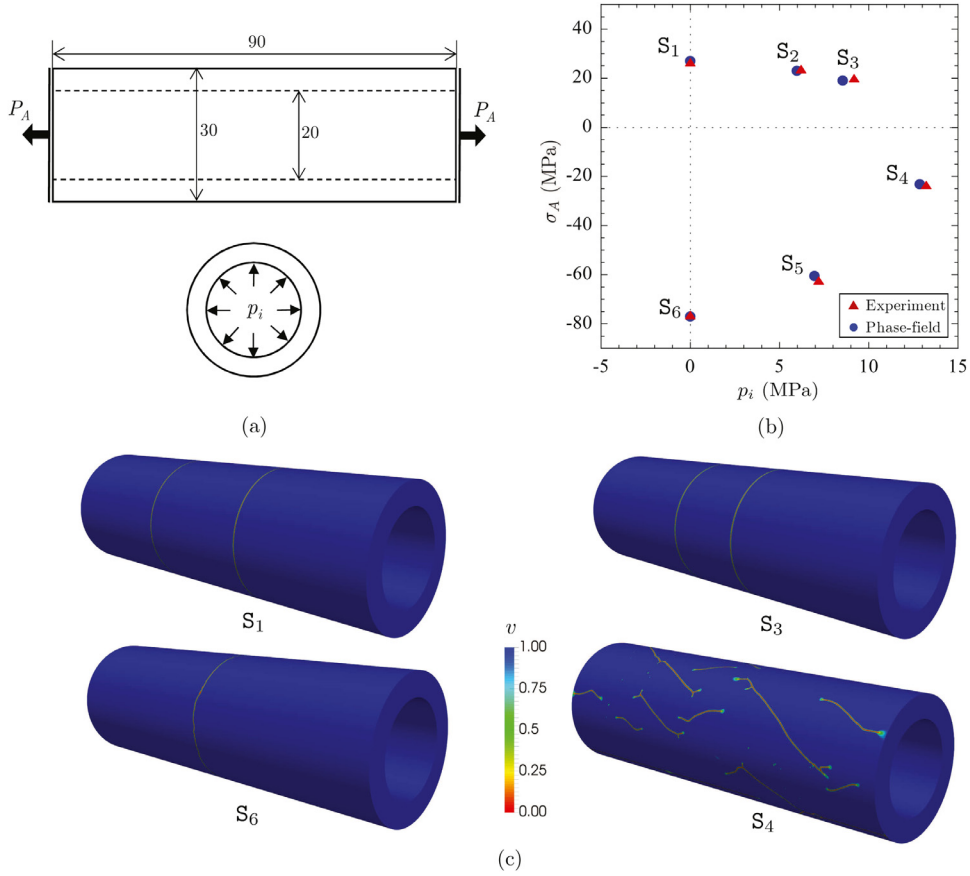


Fig. 11. Comparisons between the predictions of the proposed phase-field model and experiments of Sato et al. (1987) on graphite. (a) Schematic of the initial specimen geometry and applied boundary conditions; all sizes are indicated in mm. (b) Plot of the predicted and experimentally measured axial stress σ_A and internal pressure p_i at which fracture nucleates in six different specimens (labeled $S_1, S_2, S_3, S_4, S_5, S_6$) subjected to four different combinations of axial force P_A and internal pressure p_i . (c) Contour plots of the phase field v for specimens S_1, S_3, S_4, S_6 at the corresponding nucleation loads.

The particular graphite used in the experiments, named IG-11, was reported to have material constants $\sigma_{ts} = 27$ MPa, $\sigma_{cs} = 77$ MPa, and $G_c = 91$ N/m. Sato et al. (1987) did not include the values of the elastic constants in their material description, but those are available from other sources in the literature. Here, as already declared in Table 1, we make use of the Young's modulus $E = 9.8$ GPa and Poisson's ratio of $\nu = 0.13$ reported by Goggin and Reynolds (1967). In view of the dimensions of the tubes, we choose the localization length $\varepsilon = 0.25$ mm, which is sufficiently small. The simulations are carried out by applying displacement boundary conditions on the inner radius, top, and bottom of the tube and by making use of a uniform unstructured mesh of size $h = \varepsilon/5 = 0.05$ mm and linear tetrahedral finite elements. For the above-specified parameters, following the procedure laid out in Subsection 4.3.2, the coefficient δ^ε in the external driving force (19) takes the value 1.45.

Fig. 11(b) shows comparisons between the loads at which fracture nucleates in the tubes measured experimentally (solid triangles) and the corresponding predictions generated by the phase-field model (solid circles). The results are presented in the space of axial stress $\sigma_A = P_A/(\pi(r_o^2 - r_i^2))$ and internal pressure p_i and correspond to six different specimens, S_1, S_2, S_3, S_4, S_5 , and S_6 . Specimens S_1 and S_6 were subjected, respectively, to uniaxial tension and compression in the absence of internal pressure. On the other hand, specimens S_2 and S_3 were subjected to uniaxial tension combined with internal pressure, while specimens S_4 and S_5 were subjected to uniaxial compression combined with internal pressure.

For completeness, Fig. 11(c) presents contour plots of the phase field v for specimens S_1, S_3, S_4, S_6 at their respective loads at which fracture nucleates. We emphasize that these contour plots are representative and not unique. Computationally, this is because the stress fields for specimens S_1 and S_6 are uniform while those for S_3 and S_4 are radially symmetric and as a result different unstructured meshes can lead to the nucleation of cracks in different parts of the specimen; irrespectively of the mesh utilized for a given specimen, however, the geometries of the nucleated cracks are always qualitatively similar and, more importantly, the cracks nucleate at roughly the same critical loads. In the experiments, different specimens under the same loading conditions exhibit as well differences in the location of crack nucleation. Physically, this is because the inherent microscopic defects from where macroscopic fracture nucleates exhibit a stochastic spatial variation

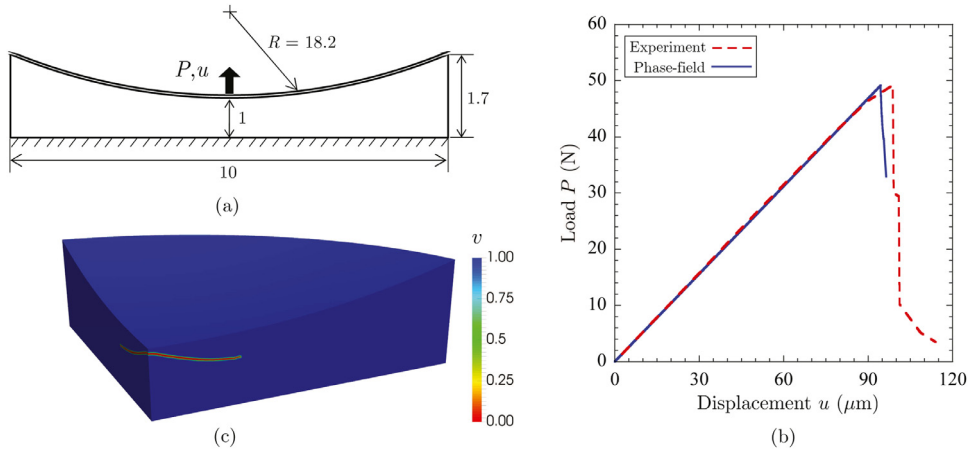


Fig. 12. Comparisons between the predictions of the proposed phase-field model and an experiment of [Cristiano et al. \(2010\)](#) on PU. (a) Schematic of the initial specimen geometry and applied boundary conditions; all sizes are indicated in mm. (b) Plot of the predicted and experimentally measured load P as a function of the applied displacement u . (c) Contour plot of the phase field v at the applied displacement $u = 97.6 \mu\text{m}$.

even within a given specimen. This stochasticity can be incorporated in the proposed phase-field model by choosing the strength material constants, σ_{ts} and σ_{cs} in the case of the external driving force (19), not to take on deterministic values but to vary randomly in space over the domain Ω occupied by the material. We do not include examples of such spatially perturbed strength material constants here but refer the interested reader to Section 7 in [Kumar et al. \(2018a\)](#), Section 4 in [Kumar et al. \(2018b\)](#), and Section 5 in [Kumar and Lopez-Pamies \(2020\)](#) for examples in the context of nucleation of fracture in silicone rubbers.

The experiment on PU. In the spirit of the classical poker-chip experiments of [Gent and Lindley \(1959\)](#), [Cristiano et al. \(2010\)](#) carried out experiments at different temperatures on poker-chip-type specimens made of PU elastomers featuring various underlying polymer chain lengths and entanglements. We focus here on the experiment at the highest temperature of 100 °C on the PU labeled PU4000. Because of its relatively short polymer chains and lack of entanglements, that type of PU exhibits essentially a linear elastic brittle response, specially at the elevated temperature of 100 °C ([Cristiano et al., 2011](#)). We remark that because of the strong confinement of the poker-chip-type geometry together with the near incompressibility of PU, the strains involved in the experiment are very small prior to fracture nucleation. On the other hand, the hydrostatic part of the stresses is tensile and large. This falls squarely within the point illustrated by [Fig. 5](#).

[Fig. 12\(a\)](#) depicts a schematic of the geometry of the poker-chip-type specimen employed by [Cristiano et al. \(2010\)](#) – a circular disk of initial diameter 10 mm and radially increasing thickness fabricated between a flat glass substrate and a glass sphere of radius 18.2 mm – and of the applied loads. These authors reported that the PU4000 elastomer at 100 °C had Young's modulus and critical energy release rate of about $E = 1.55 \text{ MPa}$ and $G_c = 41 \text{ N/m}$. While they did not provide direct measurements of the Poisson's ratio, this can be deduced from the linear elastic part in their tests. It turns out to be $\nu = 0.497$. They did not provide data regarding the strength either. Based on earlier work ([Smith, 1974](#)), we set the tensile and compressive strengths to $\sigma_{ts} = 2 \text{ MPa}$ and $\sigma_{cs} = 2.75 \text{ MPa}$. We also set the localization length to $\varepsilon = 0.01 \text{ mm}$ which results in the coefficient δ^ε taking the value -0.16 . In our simulations, moreover, we make use of a uniform unstructured mesh of size $h = \varepsilon/3 = 0.003 \text{ mm}$ and the *non-conforming* linear tetrahedral finite elements introduced by [Crouzeix and Raviart \(1973\)](#), which are particularly suitable to deal with the near incompressibility of PU; see, e.g., Section 4.3 in [Kumar et al. \(2018a\)](#) for further details on this type of finite elements. [Fig. 12\(b\)](#) shows comparisons between the load P as a function of the applied displacement u measured experimentally (dashed line) and the prediction generated by the phase-field model (solid line). [Fig. 12\(c\)](#) shows further the contour plot of the phase field v , over a quarter of the specimen to aid visualization, at the applied displacement $u = 97.6 \mu\text{m}$ illustrating that a crack nucleates near the top spherical boundary along the centerline of the specimen and then propagates transversely to the direction of the applied load.

It is evident from the results presented in [Figs. 11](#) and [12](#) that the proposed phase-field model is indeed capable of describing and predicting nucleation of fracture in the bulk, even in material systems that are nearly incompressible; see Section 5 in a companion paper ([Kumar and Lopez-Pamies, 2020](#)) for further similar results in the context of finite deformations.

5.2. Nucleation from large pre-existing cracks: An experiment on PMMA

Next, we demonstrate the capability of the proposed phase-field model to describe and predict fracture nucleation from large pre-existing cracks – or, in other words, crack propagation – via comparisons with an experiment of [Pham et al. \(2017\)](#) on PMMA.

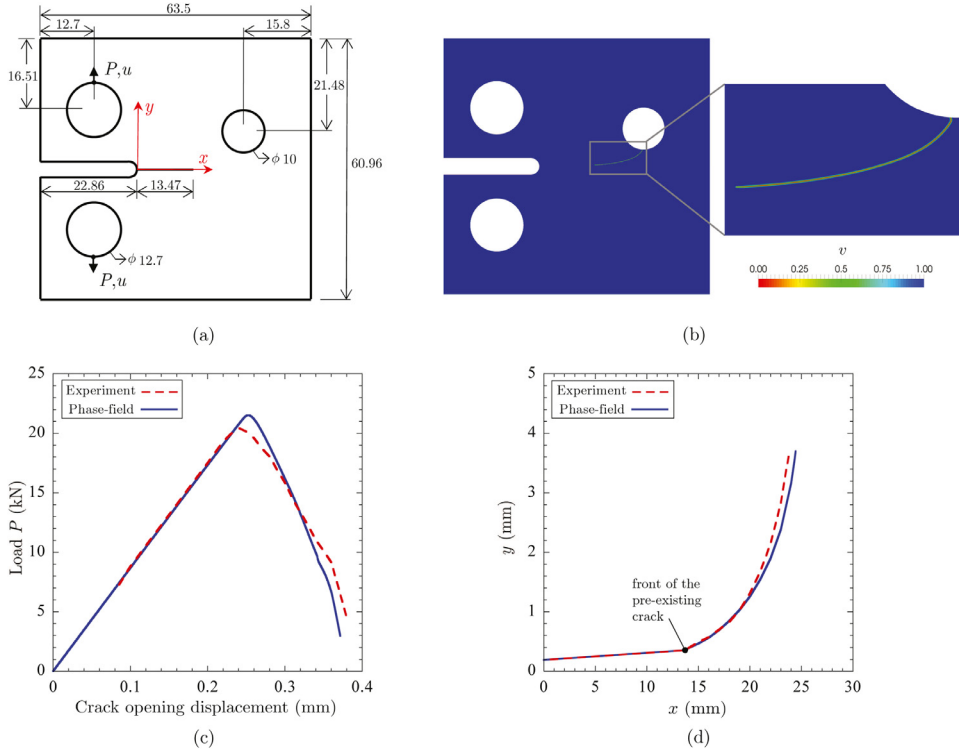


Fig. 13. Comparisons between the predictions of the proposed phase-field model and an experiment of Pham et al. (2017) on PMMA. (a) Schematic of the initial specimen geometry (thickness 3 mm) and applied boundary conditions; all sizes are indicated in mm. (b) Contour plot of the phase field v at the applied displacement $u = 0.1895$ mm. (c) Plot of the predicted and experimentally measured load P as a function of the crack opening displacement. (d) Plot of the predicted and experimentally measured crack path; note that the coordinates $(x, y) = (0, 0)$ and $(x, y) = (13.47, 0.35)$ mm correspond, respectively, to the tip of the U-notch and the front of the large pre-existing crack.

A schematic of the specimen geometry and applied loads is shown in Fig. 13(a). The PMMA was reported to have material constants $E = 2.98$ GPa, $\nu = 0.35$, $\sigma_{ts} = 50$ MPa, and $G_c = 285$ N/m. Since the value of the compressive strength was not provided by Pham et al. (2017), we set it to $\sigma_{cs} = 100$ MPa in accordance with typical values found elsewhere in the literature. Furthermore, we use the localization length $\varepsilon = 0.075$ mm, which is sufficiently small relative to the size of the specimen, and make use of a uniform unstructured mesh of size $h = \varepsilon/10 = 0.0075$ mm in our simulations, which are carried out under plane-stress conditions with linear triangular finite elements. For the above choices of the various parameters, the coefficient δ^ε in the external driving force (19) comes out to be 1.75.

Fig. 13(c) shows comparisons between the load P as a function of the crack opening displacement measured experimentally (dashed line) and the corresponding prediction generated by the phase-field model (solid line). Fig. 13(b) shows further the contour plot of the phase field v at the applied displacement $u = 0.1895$ mm; the corresponding value of the load is $P = 6.03$ kN. The crack path generated from this contour plot by tracing the points along which the phase field $v \approx 0$ is shown as a solid line in Fig. 13(d) together with the crack path obtained experimentally, shown as a dashed line. Note that in the experiment the pre-existing crack in front of the notch was not exactly aligned with the center line of the specimen (identified here with the line $y = 0$). For direct comparison, we account for the same misalignment in our simulations.

The main conclusion from the results presented in Fig. 13 is that the proposed phase-field model is capable as well of describing and predicting nucleation of fracture from large pre-existing cracks.

5.3. Nucleation from the boundary and small pre-existing cracks: Experiments on PMMA and alumina

Finally, we demonstrate the descriptive and predictive capabilities of the proposed phase-field model for the case when fracture nucleation takes places in the transition zone. We do so by means of comparisons with experiments due to Gomez et al. (2009) on PMMA at -60°C where fracture nucleates from a sharp corner and with the experiments due to Kimoto et al. (1985), already referenced in Subsection 2.3, on alumina specimens where fracture nucleates from a small pre-existing crack.

The experiments on PMMA. The geometry of the specimen and the applied loads are schematically depicted in Fig. 14(a). Because of the low temperature at which the experiments were conducted, the PMMA was reported to have material constants $E = 5.05$ GPa, $\nu = 0.40$, $\sigma_{ts} = 128$ MPa, and $G_c = 480$ N/m, which are notably different from the typical values at

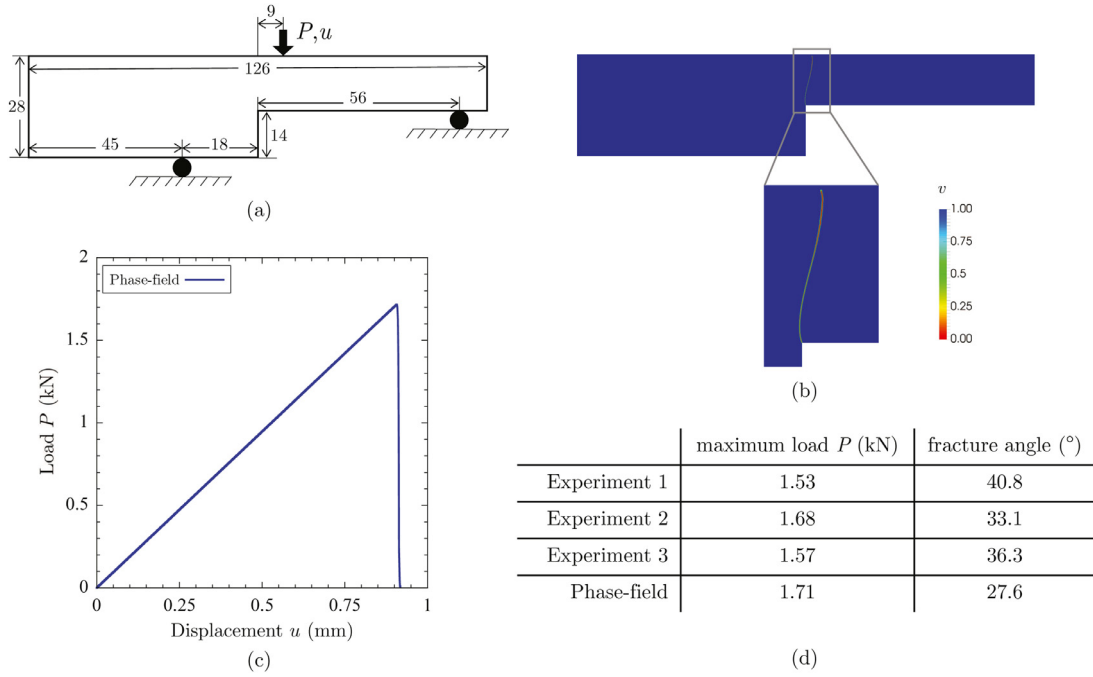


Fig. 14. Comparisons between the predictions of the proposed phase-field model and experiments of [Gomez et al. \(2009\)](#) on PMMA at -60°C . (a) Schematic of the initial specimen geometry (thickness 14 mm) and applied boundary conditions; all sizes are indicated in mm. (b) Contour plot of the phase field v at the applied displacement $u = 0.907$ mm. (c) Plot of the predicted load P as a function of the applied displacement u . (d) Table of the predicted and experimentally measured values for the maximum load P and initial fracture angle at nucleation for all three experiments reported.

room temperature. Since the compressive strength was not provided, we set its value at $\sigma_{cs} = 256$ MPa. In our simulation, carried out under conditions of plane stress with linear triangular finite elements, we set the value of the localization length to $\varepsilon = 0.05$ mm, which is sufficiently small compared to the dimensions of the specimen, and employ a uniform unstructured mesh of size $h = \varepsilon/5 = 0.01$ mm throughout the central region of the specimen where fracture is expected to nucleate and propagate. For the above choices of parameters, the appropriate value of the coefficient δ^{ε} in the external driving force (19) is found to be 0.5.

Fig. 14 (d) shows comparisons between the maximum loads P and fracture angles at nucleation measured from the three different experiments reported by [Gomez et al. \(2009\)](#) with the predictions generated by the phase-field model. For completeness, even though the corresponding experimental results are not available for comparison, **Figs. 14(c)** and **(b)** also show the load P as a function of the applied displacement u and the associated contour plot of the phase field v at the applied displacement $u = 0.907$ mm, as predicted by the phase-field model. The latter illustrates that a single crack nucleates from the sharp inner corner of the specimen and then propagates vertically severing the specimen into two pieces.

The experiments on alumina. **Fig. 15(a)** shows a schematic of the single-edge-notch specimen geometry and applied boundary conditions utilized by [Kimoto et al. \(1985\)](#). The alumina was reported to have material constants $E = 335$ GPa, $\nu = 0.25$, $\sigma_{ts} = 210$ MPa, and $G_c = 26.8$ N/m. Since the value of the compressive strength was not provided by [Kimoto et al. \(1985\)](#), we set it to $\sigma_{cs} = 2100$ MPa, which is one of the typical values reported elsewhere in the literature. The remainder of the material and computational parameters used in our simulations, carried out under plane-stress conditions with linear triangular finite elements, are $\varepsilon = 0.04$ mm, $h = \varepsilon/10 = 0.004$ mm, and $\delta^{\varepsilon} = 6.73$.

Fig. 15(b) shows comparisons between the critical values σ_{cr} of the applied stress at which fracture nucleates from the pre-existing crack measured experimentally (solid circles) and the corresponding predictions generated by the phase-field model (solid line). The results are plotted in terms of the size a of the pre-existing crack, which in the experiments was varied from $a = 0.80$ μm to $a = 0.55$ mm.

The results presented by **Figs. 14** and **15** demonstrate that the proposed phase-field model is capable as well of describing and predicting nucleation of fracture from boundary points and small pre-existing cracks.

6. Final comments

While the theory presented in [Section 4](#) might not necessarily be the final word on the matter, the sample simulations presented in [Section 5](#) certainly provide ample motivation to continue investigating the proposed phase-field model as an appropriate framework for the description of fracture nucleation and propagation in elastic brittle materials at large.

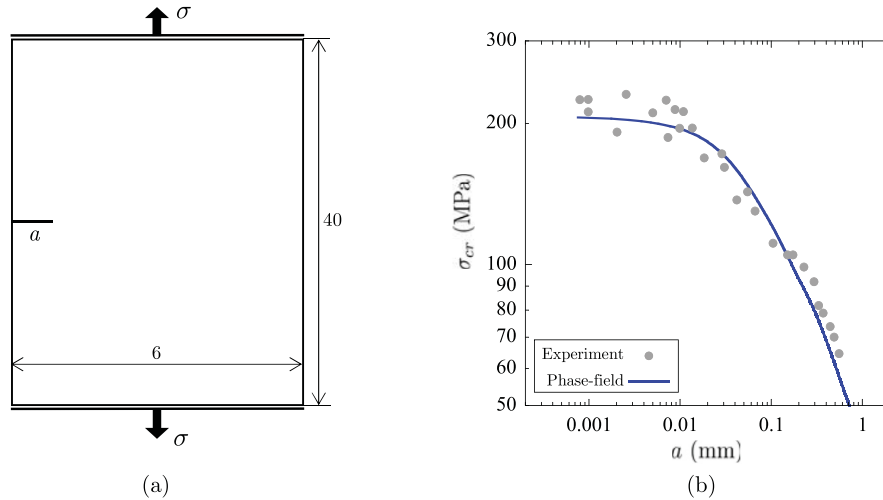


Fig. 15. Comparisons between the predictions of the proposed phase-field model and the experiments of Kimoto et al. (1985) on alumina. (a) Schematic of the initial specimen geometry (thickness 5 mm) and applied boundary conditions; all sizes are indicated in mm. (b) Plot of the predicted and experimentally measured critical stress σ_{cr} at which fracture nucleates from the small pre-existing crack as a function of its size a .

An obvious next step is to confront the model with a larger set of experiments in order to further scrutinize its predictive capabilities.

It would behoove us to study the effect of the presence of the driving force c_e on the so-called non-interpenetration phenomenon. It has been known since their inception that phase-field models of the form (2) allow for the propagation of cracks in compression. To remedy this drawback, numerous authors have proposed to consider phase-field regularizations of (1) where only a “tensile” part $W^+(\mathbf{E}(\mathbf{u}))$ of the elastic energy $W(\mathbf{E}(\mathbf{u}))$ is multiplied by the degradation function $\psi(v)$; see, e.g., Lancioni and Royer-Carfigni (2009), Amor et al. (2009), Miehe et al. (2010), Chambolle et al. (2018). Preliminary numerical simulations indicate that the driving force c_e — which has built-in the tension/compression asymmetry of the strength of the material under consideration — can prevent spurious nucleation of compressive cracks without having to resort to such an energy split.

Yet another direction of interest is the construction of driving forces more elaborate than (19) that can be calibrated for arbitrarily large localization lengths ε with the ultimate objective of being able to simulate fracture in large structures in a computationally accessible manner. Such more elaborate driving forces, if they exist, likely involve terms of $O(\varepsilon^0)$ that depend on the stress invariants I_1 and J_2 .

From a more fundamental point of view, the primary open problem is that of determining whether a limit model of sharp fracture does indeed exist in the limit as $\varepsilon \searrow 0$ of the proposed phase-field model, as suggested by numerical results.

We close by mentioning an alternative approach that could possibly incorporate the basic ingredients, the elasticity, the strength, and the critical energy release rate, in the modeling of fracture nucleation. It is that of the phase-field formulations of sharp cohesive fracture models. While there remain theoretical and practical issues yet to be addressed, some progress has been recently made on that front; see, e.g., Conti et al. (2016), Focardi and Iurlano (2017), and Wu and Nguyen (2018).

Declaration of interests

The authors declare that they have no known competing financial interests or personal relationships that could have appeared to influence the work reported in this paper.

Acknowledgements

This work was funded by the National Science Foundation through the collaborative Grants DMS-1615661 and DMS-1615839. This support is gratefully acknowledged. OLP and BB also gratefully acknowledge support from the Grants CMMI-1901583 and DMS-1716763. The seed for this work was planted during the workshop “Phase-Field Models of Fracture (19w5207)” held at the Banff International Research Station for Mathematical Innovation and Discovery (BIRS) from the 3rd to the 8th of March, 2019. The authors wish to express their gratitude to the BIRS administration, staff, and financial backers for making this workshop possible.

Appendix A. Stability of spatially homogeneous solutions: the case of no driving force

We consider the minimization problem (2) for the special case of affine displacement $\bar{\mathbf{u}}(\mathbf{x}, t) = t\bar{\mathbf{E}}\mathbf{x}$ applied on the entirety of the boundary $\partial\Omega$, where $\bar{\mathbf{E}}$ is an arbitrary constant symmetric second-order tensor. This we do for the specific choice of functions $\psi(v) = v^2$ and $s(v) = 1 - v$. Precisely, we investigate whether spatially affine/homogeneous solution pairs $(\mathbf{u}(\mathbf{x}, t), v(\mathbf{x}, t))$ are stable. We do so with two different definitions of stability as detailed below.

For such a problem, it is straightforward to show that the affine displacement and the spatially homogeneous stress fields within the domain Ω occupied by the material are simply given by

$$\mathbf{u}(\mathbf{x}, t) = t\bar{\mathbf{E}}\mathbf{x}, \quad \boldsymbol{\sigma}(t) = t\nu^2(t)(2\mu\bar{\mathbf{E}} + \lambda(\text{tr}\bar{\mathbf{E}})\mathbf{I}), \quad (25)$$

while the spatially homogeneous phase field is given by

$$\nu(t) = \begin{cases} 1 & \text{if } 0 \leq t < t_f \\ \frac{3G_c}{16\epsilon t^2 W(\bar{\mathbf{E}})} & \text{if } t \geq t_f \end{cases} \quad \text{with} \quad t_f = \sqrt{\frac{3G_c}{16\epsilon W(\bar{\mathbf{E}})}}. \quad (26)$$

The “time” t_f characterizes the critical applied strain $\bar{\mathbf{E}}_f = t_f \bar{\mathbf{E}}$ at which ν ceases to be identically 1. The corresponding critical stress is given by

$$\boldsymbol{\sigma}_f = t_f(2\mu\bar{\mathbf{E}} + \lambda(\text{tr}\bar{\mathbf{E}})\mathbf{I}) = \sqrt{\frac{3G_c}{16\epsilon W(\bar{\mathbf{E}})}}(2\mu\bar{\mathbf{E}} + \lambda(\text{tr}\bar{\mathbf{E}})\mathbf{I}). \quad (27)$$

Loss of incremental stability. First, we investigate whether a perturbation of the form $(\mathbf{u}(\mathbf{x}, t) + \xi t\mathbf{z}(\mathbf{x}), \nu(t) + \xi w(\mathbf{x}))$ with $\mathbf{z} \equiv \mathbf{0}$ on $\partial\Omega$ and $w \leq 0$ in Ω can lead to a lower energy – that is, a lower value of \mathcal{E}^ϵ than that at $(\mathbf{u}(\mathbf{x}, t), \nu(t))$ – for a small enough $\xi > 0$. This characterizes a certain loss of incremental stability. We demonstrate below that such a loss of stability does indeed occur at $t = t_f$.

For $t < t_f$ it is easily seen that stability cannot be lost for $\xi > 0$ small enough because the linear term in ξ in the expansion of $\mathcal{E}^\epsilon(\mathbf{u}(\mathbf{x}, t) + \xi t\mathbf{z}(\mathbf{x}), \nu(t) + \xi w(\mathbf{x}))$ is

$$2(t^2 - t_f^2)W(\bar{\mathbf{E}}) \int_{\Omega} w \, d\mathbf{x} > 0$$

if $w \leq 0$ is not identically 0. For $t \geq t_f$, the linear term in ξ is always 0.

Expanding $\mathcal{E}^\epsilon(\mathbf{u}(\mathbf{x}, t_f) + \xi t_f \mathbf{z}(\mathbf{x}), \nu(t_f) + \xi w(\mathbf{x}))$ and taking (26) into account and after some algebra that uses that

$$W(\bar{\mathbf{E}}) = \frac{1}{2} \bar{\mathbf{E}} \cdot \mathbf{L} \bar{\mathbf{E}} = \frac{1}{2} E_{ij} L_{ijkl} E_{kl},$$

we get

$$\begin{aligned} \mathcal{E}^\epsilon(\mathbf{u}(\mathbf{x}, t_f) + \xi t_f \mathbf{z}(\mathbf{x}), \nu(t_f) + \xi w(\mathbf{x})) &= \mathcal{E}^\epsilon(\mathbf{u}(\mathbf{x}, t_f), \nu(t_f)) + \xi^2 \left\{ \frac{3G_c}{8} \epsilon \int_{\Omega} \nabla w \cdot \nabla w \, d\mathbf{x} + \right. \\ &\quad \left. \frac{t_f^2}{2} \int_{\Omega} [\mathbf{E}(\mathbf{z}) \cdot \mathbf{L} \mathbf{E}(\mathbf{z}) + 4w\bar{\mathbf{E}} \cdot \mathbf{L} \mathbf{E}(\mathbf{z}) + w^2\bar{\mathbf{E}} \cdot \mathbf{L} \bar{\mathbf{E}}] \, d\mathbf{x} \right\}. \end{aligned} \quad (28)$$

We propose to minimize the second integral in the right hand-side of (28). Since \mathbf{L} is a positive definite fourth-order tensor with major and minor symmetries, $\bar{\mathbf{E}} \cdot \mathbf{L} \bar{\mathbf{E}} > 0$. For any fixed \mathbf{z} in $H_0^1(\Omega; \mathbb{R}^N)$,

$$w := -2 \frac{[\bar{\mathbf{E}} \cdot \mathbf{L} \mathbf{E}(\mathbf{z})]^+}{\bar{\mathbf{E}} \cdot \mathbf{L} \bar{\mathbf{E}}}$$

minimizes that integral among all $w \leq 0$'s. We are left with the minimization over $H_0^1(\Omega; \mathbb{R}^N)$ of

$$\int_{\Omega} \left[\mathbf{E}(\mathbf{z}) \cdot \mathbf{L} \mathbf{E}(\mathbf{z}) - 4 \frac{([\bar{\mathbf{E}} \cdot \mathbf{L} \mathbf{E}(\mathbf{z})]^+)^2}{\bar{\mathbf{E}} \cdot \mathbf{L} \bar{\mathbf{E}}} \right] d\mathbf{x}. \quad (29)$$

In the case of $N = 1$ space dimension, it is trivial that (29) can be made negative and even as small as we want. Next, we demonstrate it in dimension $N = 3$ and note that the same approach applies to dimension $N = 2$.

Setting without loss of generality the applied affine strain to $\bar{\mathbf{E}} = \sum_i \bar{e}_i \mathbf{e}_i \otimes \mathbf{e}_i$, with $\bar{e}_1 \geq \bar{e}_2 \geq \bar{e}_3$ and $\{\mathbf{e}_i\}$ ($i = 1, 2, 3$) denoting the principal strains and associated orthonormal principal directions, we rewrite expression (29) as

$$\int_{\Omega} \left[\lambda(\text{div} \mathbf{z})^2 + 2\mu \mathbf{E}(\mathbf{z}) \cdot \mathbf{E}(\mathbf{z}) - 4 \frac{\left(\left[\lambda(\sum_i \bar{e}_i) \text{div} \mathbf{z} + 2\mu(\sum_i \bar{e}_i \frac{\partial z_i}{\partial x_i}) \right]^+ \right)^2}{\lambda(\sum_i \bar{e}_i)^2 + 2\mu \sum_i \bar{e}_i^2} \right] d\mathbf{x}. \quad (30)$$

Now assume that $\Omega =]-a, a[^3$ and choose \mathbf{z}_n to be

$$\mathbf{z}_n(\mathbf{x}) = U(nx_1)V_2(x_2)V_3(x_3)\mathbf{e}_1$$

with $t \mapsto U(t)$, $V_i(t)$ smooth on $[-a, a]$ and 0 at $\pm a$, so that $\mathbf{z}_n \in C^\infty(]-a, a[^3)$ and $\mathbf{z}_n \equiv 0$ on $\partial\Omega$. We further choose, for δ small enough,

$$U'(t) = \begin{cases} 1/\delta, & -a \leq t \leq -a + \delta \\ -1/(2a - \delta), & -a + \delta \leq t \leq a \end{cases}, \quad V_2, V_3 \geq 0 \text{ on } [-a, a]$$

and repeat U periodically over \mathbb{R} . Then,

$$\nabla \mathbf{z}_n = nU'(nx_1)V_2(x_2)V_3(x_3)\mathbf{e}_1 \otimes \mathbf{e}_1 + U(nx_1)(V_2'(x_2)V_3(x_3)\mathbf{e}_1 \otimes \mathbf{e}_2 + V_2(x_2)V_3'(x_3)\mathbf{e}_1 \otimes \mathbf{e}_3).$$

With this, and taking without loss of generality $3\bar{e}_1 \geq \bar{e}_1 + \bar{e}_2 + \bar{e}_3$, the term $\lambda(\sum_i \bar{e}_i) + 2\mu\bar{e}_1$ is nonnegative, (30) becomes

$$\begin{aligned} & \int_{\Omega} \left[n^2(\lambda + 2\mu)(U')^2(nx_1)V_2^2(x_2)V_3^2(x_3) - 4n^2 \frac{(\lambda(\sum_i \bar{e}_i) + 2\mu\bar{e}_1)^2}{\lambda(\sum_i \bar{e}_i)^2 + 2\mu(\sum_i \bar{e}_i^2)} ([U']^+)^2(nx_1)V_2^2(x_2)V_3^2(x_3) \right. \\ & \quad \left. + \mu U^2(nx_1)\{(V_2')^2(x_2)V_3^2(x_3) + (V_3')^2(x_3)V_2^2(x_2)\} \right] d\mathbf{x} \\ &= n^2 \left((\lambda + 2\mu) \int_{-a}^a (U')^2 dt - 4 \frac{(\lambda(\sum_i \bar{e}_i) + 2\mu\bar{e}_1)^2}{\lambda(\sum_i \bar{e}_i)^2 + 2\mu(\sum_i \bar{e}_i^2)} \int_{-a}^a ([U']^+)^2 dt \right) \int_{-a}^a V_2^2 dt \int_{-a}^a V_3^2 dt \\ & \quad + \mu \int_{-a}^a U^2 dt \left\{ \int_{-a}^a (V_2')^2 dt \int_{-a}^a V_3^2 dt + \int_{-a}^a (V_3')^2 dt \int_{-a}^a V_2^2 dt \right\} =: I_n. \end{aligned}$$

But

$$\int_{-a}^a (U')^2 dt = 1/\delta + 1/(2a - \delta), \quad \int_{-a}^a ([U']^+)^2 dt = 1/\delta,$$

so that I_n becomes

$$\begin{aligned} I_n &= n^2 \left[\frac{1}{\delta} \left((\lambda + 2\mu) - 4 \frac{(\lambda(\sum_i \bar{e}_i) + 2\mu\bar{e}_1)^2}{\lambda(\sum_i \bar{e}_i)^2 + 2\mu(\sum_i \bar{e}_i^2)} \right) + \frac{(\lambda + 2\mu)}{2a - \delta} \right] \int_{-a}^a V_2^2 dt \int_{-a}^a V_3^2 dt \\ & \quad + \mu \int_{-a}^a U^2 dt \left\{ \int_{-a}^a (V_2')^2 dt \int_{-a}^a V_3^2 dt + \int_{-a}^a (V_3')^2 dt \int_{-a}^a V_2^2 dt \right\}. \end{aligned}$$

Now, a tedious check would demonstrate that the term

$$(\lambda + 2\mu) - 4 \frac{(\lambda(\sum_i \bar{e}_i) + 2\mu\bar{e}_1)^2}{\lambda(\sum_i \bar{e}_i)^2 + 2\mu(\sum_i \bar{e}_i^2)}$$

is strictly negative for all values of $\bar{e}_1, \bar{e}_2, \bar{e}_3$, provided that $\lambda \neq 0$. If $\lambda = 0$, that term is easily seen to be strictly negative. So I_n can clearly be made negative, and even as small as we want, through an adequate choice of $\delta < 1$.

By taking a to be such that $]-a, a[^3 \subset \subset \Omega$ we have shown that, for n large enough, (29) can be made strictly negative for some pair w, \mathbf{z}_n in $L^2(\Omega) \times H_0^1(\Omega; \mathbb{R}^3)$ with $w(x) \leq 0$ on $]-a, a[^3$. Then, going back to (28), the term in ξ^2 can be made strictly negative provided that ε is small enough through the above choice of w and \mathbf{z}_n . Algebra, together with relation (7) as well as the identities $\kappa = \lambda + 2\mu/3$ and $E = 9\mu\kappa/(\mu + 3\kappa)$ in dimension $N = 3$ leads to (8) for any σ_ε given by expression (27).

Remark that we have merely described a particular type of loss of stability and not the onset of localization. Ideally, one would carry out a bifurcation analysis of the problem (2) in order to determine that at “time” $t = t_\varepsilon$ the homogeneous solution (25)–(26) does bifurcate into a heterogeneous solution wherein the phase field v localizes. We limit our study to complementing the above incremental stability analysis with the analysis of another type of loss of stability, that characterized by the loss of strong ellipticity of the stress-strain relation (25)₂, and conclude that, provided $\lambda > -2/9\mu$, both types lead to the same critical stresses (8).

Loss of strong ellipticity. Note from (25)₂ and (26) that

$$\boldsymbol{\sigma} = \begin{cases} t(2\mu\bar{\mathbf{E}} + \lambda(\text{tr}\bar{\mathbf{E}})\mathbf{I}) & \text{if } 0 \leq t < t_\varepsilon \\ \frac{1}{t^3} \left(\frac{3G_c}{16\varepsilon W(\bar{\mathbf{E}})} \right)^2 (2\mu\bar{\mathbf{E}} + \lambda(\text{tr}\bar{\mathbf{E}})\mathbf{I}) & \text{if } t \geq t_\varepsilon \end{cases} \quad (31)$$

and recall that a nonlinear elastic stress-strain relation of the form $\boldsymbol{\sigma} = \hat{\boldsymbol{\sigma}}(\bar{\mathbf{E}})$, such as (31), is strongly elliptic when

$$\min_{\|\mathbf{a}\|=\|\mathbf{b}\|=1} \{a_j b_j \hat{L}_{ijkl}(\bar{\mathbf{E}}) a_k b_l\} > 0 \quad \text{with} \quad \hat{L}_{ijkl}(\bar{\mathbf{E}}) = \frac{\partial \hat{\sigma}_{ij}}{\partial \bar{E}_{kl}}(\bar{\mathbf{E}}).$$

Now, for isotropic stress-strain relations such as (31), the loss of strong ellipticity can be written exclusively in terms of the components of the incremental modulus of elasticity $\hat{L}_{ijkl}(\bar{\mathbf{E}})$ written in the axes of principal strain; see, e.g., Dacorogna (2001) and Appendix A in Lopez-Pamies and Ponte Castañeda (2007). Here, setting $\bar{\mathbf{E}} = \text{diag}(\bar{e}_1, \dots, \bar{e}_3)$, we get as necessary and sufficient conditions for strong ellipticity:

$$\hat{L}_{iiii}(\bar{\mathbf{E}}) > 0, \quad i = 1, \dots, N \quad (32)$$

and

$$\hat{L}_{iiii}(\bar{\mathbf{E}})\hat{L}_{jjjj}(\bar{\mathbf{E}}) + \hat{L}_{ijji}^2(\bar{\mathbf{E}}) - (\hat{L}_{ijij}(\bar{\mathbf{E}}) + \hat{L}_{ijji}(\bar{\mathbf{E}}))^2 + 2\hat{L}_{ijij}(\bar{\mathbf{E}})\sqrt{\hat{L}_{iiii}(\bar{\mathbf{E}})\hat{L}_{jjjj}(\bar{\mathbf{E}})} > 0, \quad 1 \leq i < j \leq N, \quad (33)$$

where repeated indices do not imply summation.

Now, the incremental modulus of elasticity of the stress-strain relation (31) is given by

$$\hat{L}_{ijkl}(\bar{\mathbf{E}}) = \begin{cases} t(\mu(\delta_{ik}\delta_{jl} + \delta_{il}\delta_{jk}) + \lambda\delta_{ij}\delta_{kl}) & \text{if } 0 \leq t < t_\ell \\ \frac{1}{t^3} \left(\frac{3G_c}{16\varepsilon W(\bar{\mathbf{E}})} \right)^2 (\mu(\delta_{ik}\delta_{jl} + \delta_{il}\delta_{jk}) + \lambda\delta_{ij}\delta_{kl} - \frac{2}{W(\bar{\mathbf{E}})} (4\mu^2\bar{E}_{ij}\bar{E}_{kl} + 2\mu\lambda\bar{E}_{mm}(\delta_{ij}\bar{E}_{kl} + \bar{E}_{ij}\delta_{kl}) + \lambda^2(\bar{E}_{mm})^2\delta_{ij}\delta_{kl})) & \text{if } t \geq t_\ell \end{cases} \quad (34)$$

One can check that, provided that $\mu > 0$ and $\lambda > -2/9\mu$, (34) ceases to be strongly elliptic precisely at $t = t_\ell$, and remains so for $t > t_\ell$ because at least one of the conditions (32)–(33) fails for any choice of strain $\bar{\mathbf{E}} = \text{diag}(\bar{e}_1, \dots, \bar{e}_N)$.

Appendix B. Stability of spatially homogeneous solutions: the case with driving force

Consider the equations (11)–(12) with external driving force of the form (14) in the case of an affine displacement $\bar{\mathbf{u}}(\mathbf{x}, t) = \bar{\mathbf{E}}(t)\mathbf{x}$ prescribed on all of $\partial\Omega$. In the vein of Appendix A, we take the phase field v to be homogeneous. It is then a simple matter to deduce that the displacement, strain, and stress fields throughout the material are given by

$$\mathbf{u}(\mathbf{x}, t) = \bar{\mathbf{E}}(t)\mathbf{x}, \quad \mathbf{E}(t) = \bar{\mathbf{E}}(t), \quad \boldsymbol{\sigma}(t) = 2\mu\nu^2\bar{\mathbf{E}}(t) + \left(\kappa - \frac{2\mu}{3}\right)\nu^2(\text{tr}\bar{\mathbf{E}}(t))\mathbf{I}. \quad (36)$$

Furthermore, the phase field v is identically 1 from the initial “time” $t = 0$ up to the critical “time” $t = t_\ell$ at which it ceases to be identically so. From (12)₂, it follows that that critical “time” is given by the smallest positive root of the nonlinear algebraic equation

$$\mathcal{T}(t_\ell) = 1 - \frac{3G_c}{16\varepsilon W(\bar{\mathbf{E}}(t_\ell))} - \frac{\hat{c}_e(\bar{I}_1(t_\ell), \bar{J}_2(t_\ell); \varepsilon)}{2W(\bar{\mathbf{E}}(t_\ell))} = 0,$$

where, for convenience, we have introduced the notation

$$\bar{I}_1(t) = 3\kappa \text{tr}\bar{\mathbf{E}}(t) \quad \text{and} \quad \bar{J}_2(t) = 2\mu^2 \text{tr}\bar{\mathbf{E}}_D^2(t) \quad \text{with} \quad \bar{\mathbf{E}}_D(t) = \bar{\mathbf{E}}(t) - \frac{1}{3}(\text{tr}\bar{\mathbf{E}}(t))\mathbf{I}.$$

For “times” $t > t_\ell$, on the other hand, the phase field is defined implicitly by the condition

$$\mathcal{V}(v; \bar{\mathbf{E}}(t)) = v - \frac{3G_c}{16\varepsilon W(\bar{\mathbf{E}}(t))} - \frac{\hat{c}_e(\nu^2\bar{I}_1, \nu^4\bar{J}_2; \varepsilon)}{2W(\bar{\mathbf{E}}(t))} = 0. \quad (37)$$

For most choices of the external driving force \hat{c}_e , the nonlinear algebraic Eq. (37) is not expected to admit an explicit solution for v . We then rewrite (37) in terms of the stress (36)₃. Inverting relation (36)₃ yields

$$\bar{\mathbf{E}}(t) = \frac{1}{2\nu^2\mu}\boldsymbol{\sigma}(t) + \frac{1}{3\nu^2}\left(\frac{1}{3\kappa} - \frac{1}{2\mu}\right)(\text{tr}\boldsymbol{\sigma}(t))\mathbf{I}$$

from which it immediately follows that the Eq. (37) for the phase field v can be rewritten as

$$\hat{\mathcal{V}}(v; I_1, J_2) = \frac{1}{\nu^3}\left(\frac{J_2}{\mu} + \frac{I_1^2}{9\kappa}\right) - \hat{c}_e(I_1, J_2; \varepsilon) - \frac{3G_c}{8\varepsilon} = 0 \quad (38)$$

in terms of the principal invariants (5)_{1–2} of the stress (36)₃. In view of (38), it is now trivial to deduce that (20) is the stress level at which the phase field v ceases to be identically 1.

One should then carry out some kind of bifurcation analysis of Eqs. (11)–(12) in order to demonstrate that the homogeneous solution identified by (38) at $t = t_\ell$ is actually unstable and additionally that it bifurcates into a heterogeneous

solution where the phase field v localizes. Here, as in the latter part of Appendix A, we investigate when the stress-strain relation (36)₃ loses strong ellipticity. This we can only do numerically at present. It seems that the stress-strain relation (36)₃ does lose strong ellipticity at the critical uniform stresses σ defined by (20) and further that the phase field v does localize precisely then.

References

- Alessi, R., Vidoli, S., De Lorenzis, L., 2018. A phenomenological approach to fatigue with a variational phase-field model: the one-dimensional case. *Eng. Fract. Mech.* 190, 53–73.
- Amor, H., Marigo, J.-J., Maurini, C., 2009. Regularized formulation of the variational brittle fracture with unilateral contact: numerical experiments. *J. Mech. Phys. Solids* 57, 1209–1229.
- Bažant, Z.P., 2005. *Scaling of Structural Strength*, Elsevier.
- Borden, M.J., Verhoosel, C.V., Scott, M.A., Hughes, T.J.R., Landis, C.M., 2012. A phase-field description of dynamic brittle fracture. *Comput. Methods Appl. Mech. Eng.* 217, 77–95.
- Bourdin, B., Francfort, G.A., Marigo, J.J., 2000. Numerical experiments in revisited brittle fracture. *J. Mech. Phys. Solids* 48, 797–826.
- Bourdin, B., Francfort, G.A., Marigo, J.J., 2008. The variational approach to fracture. *J. Elast.* 91, 5–148.
- Bradt, R.C., Munz, D., Sakai, M., White, K.W., 2005. *Fracture mechanics of ceramics: Active materials, nanoscale materials, composites, glass and fundamentals*. Springer.
- Braides, A., 1998. *Approximation of free-discontinuity problems*. Springer.
- Chambolle, A., Conti, S., Francfort, G.A., 2018. Approximation of a brittle fracture energy with a constraint of non-interpenetration. *Arch. Rat. Mech. Anal.* 228, 867–889.
- Conti, S., Focardi, M., Iurlano, F., 2016. Phase field approximation of cohesive fracture models. *Ann. l'Inst. Henri Poincaré (C) Non Linear Anal.* 33, 1033–1067.
- Cristiano, A., Marcellan, A., Kestran, B.J., Steeman, P., Creton, C., 2011. Fracture of model polyurethane elastomeric networks. *Journal of Polymer Science: Part B: Polymer Physics* 49, 355–367.
- Cristiano, A., Marcellan, A., Long, R., Hui, C.-Y., Stolk, J., Creton, C., 2010. An experimental investigation of fracture by cavitation of model elastomeric networks. *Journal of Polymer Science: Part B: Polymer Physics* 48, 1409–1422.
- Crouzeix, M., Raviart, P.A., 1973. Conforming and nonconforming finite element methods for solving the stationary stokes equations i. *Rev. Française Automat. Informat. Recherche Opérationnelle. Mathématique* 7, 33–75.
- Dacorogna, B., 2001. Necessary and sufficient conditions for strong ellipticity of isotropic functions in any dimension. *Discrete Contin. Dyn. Syst. Ser. B* 1, 257–263.
- Drucker, D.C., Prager, W., 1952. Soil mechanics and plastic analysis for limit design. *Q. Appl. Math.* 10, 157–165.
- Dunn, M.L., Suwito, W., Cunningham, S., 1997. Fracture initiation at sharp notches: correlation using critical stress intensities. *Int. J. Solids Struct.* 34, 3873–3883.
- Ely, R.E., 1972. Strength of titania and aluminum silicate under combined stresses. *J. Am. Ceram. Soc.* 55, 347–350.
- Focardi, M., Iurlano, F., 2017. Numerical insight of a variational smeared approach to cohesive fracture. *J. Mech. Phys. Solids* 98, 156–171.
- Francfort, G.A., Marigo, J.J., 1998. Revisiting brittle fracture as an energy minimization problem. *J. Mech. Phys. Solids* 46, 1319–1342.
- Gent, A.N., Lindley, P.B., 1959. Internal rupture of bonded rubber cylinders in tension. *Proc. R. Soc. A* 249, 195–205.
- Gent, A.N., Park, B., 1984. Failure processes in elastomers at or near a rigid inclusion. *J. Mater. Sci.* 19, 1947–1956.
- Giaccio, G., Zerbino, R., 1998. Failure mechanism of concrete: combined effects of coarse aggregates and strength level. *Adv. Cem. Based Mater.* 7, 41–48.
- Goggin, P.R., Reynolds, W.N., 1967. The elastic constants of reactor graphites. *Philos. Mag.* 16, 317–330.
- Gomez, F.J., Elices, M., Berto, F., Lazzarin, P., 2009. Fracture of v-notched specimens under mixed mode (I + II) loading in brittle materials. *Int. J. Fract.* 159, 121–135.
- Griffith, A.A., 1921. The phenomena of rupture and flow in solids. *Philos. Trans. R. Soc. Lond. A* 221, 163–198.
- Hossain, M.Z., Bourdin, B., Bhattacharya, K., Hsueh, C.-J., 2014. Effective toughness of heterogeneous media. *J. Mech. Phys. Solids* 71, 320–348.
- Irwin, G., 1957. Analysis of stresses and strains near the end of a crack traversing a plate. *J. Appl. Mech.* 24, 361–364.
- Irwin, G., 1958. *Fracture*. In: Flügge, S. (Ed.), *Elasticity and Plasticity*. Springer.
- Iuga, M., Steinle-Neumann, G., Meinhardt, J., 2007. Ab-initio simulation of elastic constants for some ceramic materials. *Eur. Phys. J. B* 58, 127–133.
- Kimoto, H., Usami, S., Miyata, H., 1985. Flaw size dependence in fracture stress of glass and polycrystalline ceramics. *Transactions of the Japan Society of Mechanical Engineers Series A* 51, 2482–2488.
- Kumar, A., Francfort, G.A., Lopez-Pamies, O., 2018a. Fracture and healing of elastomers: a phase-transition theory and numerical implementation. *J. Mech. Phys. Solids* 112, 523–551.
- Kumar, A., Lopez-Pamies, O., 2020. The phase-field approach to self-healable fracture of elastomers: a model accounting for fracture nucleation at large, with application to a class of conspicuous experiments. *Theor. Appl. Fract. Mech.* 107, 102550.
- Kumar, A., Ravi-Chandar, K., Lopez-Pamies, O., 2018b. The configurational-forces view of fracture and healing in elastomers as a phase transition. *Int. J. Fract.* 213, 1–16.
- Lancioni, G., Royer-Carfagni, G., 2009. The variational approach to fracture mechanics. a practical application to the french *panthéon* in paris. *J. Elasticity* 95, 1–30.
- Lefèvre, V., Ravi-Chandar, K., Lopez-Pamies, O., 2015. Cavitation in rubber: an elastic instability or a fracture phenomenon? *Int. J. Fract.* 192, 1–23.
- Lopez-Pamies, O., Ponte Castañeda, P., 2007. Homogenization-based constitutive models for porous elastomers and implications for macroscopic instabilities: I — analysis. *J. Mech. Phys. Solids* 55, 1677–1701.
- Mark, J., Erman, B., Roland, M., 2013. *The science and technology of rubber*. Academic Press.
- Mesgarnejad, A., Bourdin, B., Khonsari, M.M., 2015. Validation simulations for the variational approach to fracture. *Comp. Methods Appl. Mech. Eng.* 290, 420–437.
- Miehe, C., Welschinger, F., Hofacker, M., 2010. Thermodynamically consistent phase-field models of fracture: variational principles and multi-field FE implementations. *Int. J. Numer. Methods Eng.* 83, 1273–1311.
- Munz, D., Fett, T., 1999. *Ceramics: Mechanical properties, failure behaviour, materials selection*. Springer.
- Nguyen, T.T., Yvonnet, J., Bornert, M., Chateau, C., Sab, K., Romani, R., Le Roy, R., 2016. On the choice of parameters in the phase field method for simulating crack initiation with experimental validation. *Int. J. Fracture* 197, 213–226.
- Pham, K., Amor, H., Marigo, J.J., Maurini, C., 2011. Gradient damage models and their use to approximate brittle fracture. *Int. J. Damage Mech.* 20, 618–652.
- Pham, K.H., Ravi-Chandar, K., Landis, C.M., 2017. Experimental validation of a phase-field model for fracture. *Int. J. Fract.* 205, 83–101.
- Poulain, X., Lefèvre, V., Lopez-Pamies, O., Ravi-Chandar, K., 2017. Damage in elastomers: nucleation and growth of cavities, micro-cracks, and macro-cracks. *Int. J. Fract.* 205, 1–21.
- Poulain, X., Lopez-Pamies, O., Ravi-Chandar, K., 2018. Damage in elastomers: healing of internally nucleated cavities and micro-cracks. *Soft Matter* 14, 4633–4640.
- Rice, J.R., 1968. A path independent integral and approximate analysis of strain concentration by notches and cracks. *J. Appl. Mech.* 35, 379–386.

- Sato, S., Awaji, H., Kawamata, K., Kurumada, A., Oku, T., 1987. Fracture criteria of reactor graphite under multiaxial stresses. *Nuclear Engng. Design* 103, 291–300.
- Smith, T.L., 1974. Tensile strength of polyurethane and other elastomeric block copolymers. *Journal of Polymer Science: Polymer Physics Edition* 12, 1825–1848. 1974
- Tada, H., Paris, P.C., Irwin, G.R., 1973. The stress analysis of cracks handbook 3rd edition. The American Society of Mechanical Engineers, New York.
- Tanné, E., Li, T., Bourdin, B., Marigo, J.J., Maurini, C., 2018. Crack nucleation in variational phase-field models of brittle fracture. *J. Mech. Phys. Solids* 110, 80–99.
- Tomsia, A.P., Glaeser, A.M., 1998. Ceramic microstructures: Control at the atomic level. Springer.
- Usami, S., Kimoto, H., Takahashi, I., Shida, S., 1986. Strength of ceramic materials containing small flaws. *Eng. Fract. Mech.* 23, 745–761.
- Wu, J.-Y., Nguyen, V.P., 2018. A length scale insensitive phase-field damage model for brittle fracture. *J. Mech. Phys. Solids* 119, 20–42.
- Zehnder, A.T., 2012. Fracture mechanics. Springer.